The arrested state of processing bodies supports mRNA regulation in early development

M.Sankaranarayanan[1]*, Ryan J. Emenecker[2], Marcus Jahnel[3], Irmela R. E. A. Trussina[3], Matt Wayland[1], Simon Alberti[3], Alex S. Holehouse[2], Timothy T. Weil[1]*

[1] Department of Zoology, University of Cambridge, Downing Street, Cambridge CB2 3EJ, UK.

[2] Department of Biomedical Engineering and Center for Science and Engineering of Living Systems, Washington University in St. Louis, 1 Brookings Drive, St. Louis, MO 63130, USA.

[3] Center for Molecular and Cellular Bioengineering, Biotechnology Center, Technische Universitat Dresden, Tatzberg 47/49, 01307 Dresden, Germany.

* Correspondence: msnsankar18@gmail.com or tw419@cam.ac.uk

ABSTRACT

Biomolecular condensates that form via liquid-liquid phase separation can exhibit diverse physical states. Despite considerable progress, the relevance of condensate physical states for *in vivo* biological function remains limited. Here, we investigated the physical properties of *in vivo* processing bodies (P bodies) and their impact on mRNA storage in mature *Drosophila* oocytes. We show that the conserved DEAD-box RNA helicase Me31B forms P body condensates which adopt a less dynamic, arrested physical state. We demonstrate that structurally distinct proteins and hydrophobic and electrostatic interactions, together with RNA and intrinsically disordered regions, regulate the physical properties of P bodies. Finally, using live imaging, we show that the arrested state of P bodies is required to prevent the premature release of *bicoid* (*bcd*) mRNA, a body axis determinant, and that P body dissolution leads to *bcd* release. Together, this work establishes a role for arrested states of biomolecular condensates in regulating cellular function in a developing organism.

INTRODUCTION

Many biochemical reactions in the cytoplasm of eukaryotic cells require regulation in space and time. The organization of specific reactions in the dense cytoplasmic environment is achieved through membrane-bound and membrane-less organelles. Classic membrane-bound organelles such as the nucleus and endoplasmic reticulum are stable micro-environments enclosed by membranes. However, membrane-less organelles such as stress granules, processing bodies (P bodies) and nuclear bodies have been shown to also provide an essential, dynamic level of cellular organization (Banani *et al.*, 2017; Shin and Brangwynne, 2017; Boeynaems *et al.*, 2018) . Typically composed of ribonucleic acids (RNA) and proteins, the assembly of many membrane-less organelles is well-described via a spontaneous demixing process referred to as liquid-liquid phase separation (LLPS) (Brangwynne *et al.*, 2009; Li *et al.*, 2012; Hubstenberger *et al.*, 2013; Wang *et al.*, 2014; Nott *et al.*, 2015; Zhang *et al.*, 2015; Feric *et al.*, 2016). In its simplest instantiation, LLPS occurs when a specific set of one or more macromolecules condense into a distinct liquid-like phase that is relatively enriched for those macromolecules in comparison to the surrounding and coexisting phase (e.g., cytoplasm or nucleoplasm) (Hyman, Weber and Jülicher, 2014; Brangwynne, Tompa and Pappu, 2015; Banani *et al.*, 2017; Lyon, Peeples and Rosen, 2021). More generally, the designation *biomolecular condensates* has emerged as an overarching term to describe cellular assemblies characterized by the non-stoichiometric concentration of biomacromolecules, of which membrane-less organelles are one such example.

Ribonucleoprotein (RNP) complexes are an abundant and conserved class of biomolecular condensates. Found both in the cytoplasm and the nucleus, RNP condensates exhibit a wide range of physical states ranging from dynamic liquids to stable solids (Weber and Brangwynne, 2012; Kroschwald *et al.*, 2015, 2018; Weber, 2017; Woodruff *et al.*, 2017). Some examples of diverse physical states observed *in vivo* include liquid-like P granules in *C. elegans* embryos (Brangwynne *et al.*, 2009; Wang *et al.*, 2014); viscous, semi-liquid nucleolus in *Xenopus laevis* oocytes (Brangwynne, Mitchison and Hyman, 2011; Feric *et al.*, 2016; Mitrea *et al.*, 2016); and solid-like Balbiani bodies in the cytoplasm of vertebrate oocytes (Boke *et al.*, 2016). Despite considerable progress in our understanding of biomolecular condensates, the

relationship between condensate physical state and *in vivo* function remains poorly understood. More broadly, while the study of metazoan condensates *in vitro* and in cell culture has been instrumental in our modern understanding of their role in cellular organization and function, *in vivo* approaches are much less common. RNP condensates are often linked with localized translation which enables cells to spatiotemporally regulate protein synthesis through localization, storage and translational control of stored mRNAs (Medioni, Mowry and Besse, 2012). Specialized cells, including neurons and eggs, often rely on this mode of post transcriptional regulation to control gene expression (Kloc and Etkin, 2005; Jung *et al.*, 2014). Specifically, in transcriptionally inactive oocytes, such as *Drosophila melanogaster*, prolonged storage and translational control of maternally deposited transcripts are required for body axes patterning (Tadros and Lipshitz, 2009; Lasko, 2012).

One mechanism for regulating RNA storage and translational control involves P bodies, an evolutionarily conserved class of cytoplasmic biomolecular condensates (Andrei *et al.*, 2005; Kedersha *et al.*, 2005; Eulalio *et al.*, 2007; Parker and Sheth, 2007; Buchan, Buchan and Buchan, 2014; Hubstenberger *et al.*, 2017; Luo, Na and Slavoff, 2018). Previous work on P bodies has highlighted their roles in various aspects of RNA metabolism, including RNA storage and translational repression since P bodies are devoid of ribosomes (Weil *et al.*, 2012; Hubstenberger *et al.*, 2017). A conserved component of P bodies is the ATP-dependent DEAD box RNA helicase human DDX6, which is conserved across yeast (Dhh1), *C. elegans* (CGH-1), and *Drosophila* (Maternal expression at 31B (Me31B)). Me31B is required for early *Drosophila* development and estimated to be present at concentrations of ~7.5 µM in the egg (Götze *et al.*, 2017). During oogenesis, Me31B is known to associate with and differentially regulate several axis-patterning maternal mRNAs (Nakamura *et al.*, 2001; Weil *et al.*, 2012). The dorsoventral determinant *gurken* mRNA is translated early in oogenesis, while *bicoid* (*bcd*) mRNA is repressed and retained in the oocyte until egg activation, a conserved process that is required before entry into embryogenesis (Tadros and Lipshitz, 2009; Weil *et al.*, 2012; Kaneuchi *et al.*, 2015; York-andersen *et al.*, 2015). Failure to regulate these, and many other mRNAs can lead to severe developmental defects (Lasko, 2012). However, the mechanisms that underlie how transcripts are maintained and translationally controlled by P bodies is not well understood.

92   To examine the *in vivo* basis of mRNA regulation, we use time-lapse fluorescence
93   microscopy, genetics and pharmacological treatments to investigate the physical
94   properties and *in vivo* function of P bodies in the mature *Drosophila* oocyte. We find
95   that P body condensates adopt an arrested physical state in the mature oocyte. We
96   show that P body integrity requires weak electrostatic and hydrophobic interactions,
97   along with RNA and the actin cytoskeleton. Using *in silico* and *in vitro* approaches, we
98   demonstrate that intrinsically disordered regions (IDRs) regulate Me31B condensation
99   and their physical properties. We also find that the highly disordered protein Trailer
100 hitch (Tral) is required for the assembly and organization of P bodies. Finally, we
101 demonstrate that the condensed and arrested state of P bodies prevents the release
102 of *bicoid (bcd)* mRNA, highlighting an important cellular function of P bodies in
103 *Drosophila* and an *in vivo* role for P body physical state. Based on these results and
104 other analogous work, we propose that less dynamic, arrested physical states are a
105 universal feature of RNP condensates in specialized cells to temporally regulate RNAs
106 in response to cellular and developmental cues.

RESULTS

Me31B forms less dynamic, arrested P body condensates in the mature oocyte

Maternal mRNAs are thought to be stored and regulated by P bodies throughout oogenesis (Nakamura *et al.*, 2001; Lin *et al.*, 2008; Weil *et al.*, 2012). Egg activation of the mature oocyte, which is the final stage of oogenesis, results in the release of stored mRNAs and subsequent translation (Tadros and Lipshitz, 2009; Krauchunas and Wolfner, 2013). However, a mechanistic understanding of how the physical state of P bodies regulates mRNA remains unclear. To address this, we isolated living mature oocytes from female *Drosophila* (Figure 1A) and utilized the conserved DEAD-box RNA helicase, Me31B, to visualize P bodies (Figure 1B). Live imaging of Me31B (Me31B::GFP) revealed that P bodies are typically micron sized condensates with varying morphology and sizes (Figure 1C). We also find that most P bodies have internal subdomains indicating that they are heterogeneously organized (Figure 1D). Quantification of P body aspect ratios over time suggests that P bodies have predominantly irregular morphologies compared to liquid-like condensates which are typically spherical (Figure 1E). Additionally, P bodies undergo continuous morphological rearrangement, with most progressing from irregular to more rounded shapes (Figure 2A). Aspect ratio analysis of individual condensates followed over time showed rearrangement of P bodies relaxing from an amorphous to a round shape in 30 minutes (Figure 2A), more slowly than many previously studied liquid-like condensates (Brangwynne *et al.*, 2009; Feric *et al.*, 2016). Although P bodies undergo fusion and fission events (Figure 2B, 2B', and S1), which are a hallmark of liquid-like condensates, the longer timescale of these events indicate that P bodies in the mature *Drosophila* oocyte are less dynamic compared to known liquid-like condensates such as P granules and stress granules (Brangwynne *et al.*, 2009; Patel *et al.*, 2015).

The cytoplasm of the mature oocyte is packed with yolk granules, organelles, and complex cytoskeletal structures. To determine if the slow P body dynamics are an intrinsic property or dependent on the oocyte cytoplasmic environment, we developed an *ex vivo* assay whereby we extrude the cytoplasm into halocarbon oil (Figure 2C). Importantly, this approach does not promote P body dissolution, rather, extruded P bodies initially exhibit irregular morphologies but become spherical with time (Figure 2C'). Consistent with *in vivo* observations, we also show extruded P bodies undergo fusion and fission events over longer timescales (Figure 2D and 2D'). Taken together

140 our data suggests that P bodies are slowly rearranging viscoelastic condensates, and

141 that this physical state is inherent to P bodies from mature *Drosophila* oocytes.

142 We next performed Fluorescence Recovery After Photobleaching (FRAP) on whole P

143 bodies (whole FRAP) to examine the mobility of Me31B between the cytoplasm and P

144 body. This analysis revealed that Me31B localized to P bodies exhibited limited or no

145 recovery (Figure 2E and 2F). Due to their inability to exchange Me31B with the

146 cytoplasm, we refer to this as the arrested state of P bodies. To further explore Me31B

147 dynamics, we tested if Me31B can rearrange within P bodies by observing the

148 recovery of Me31B fluorescence after photobleaching within a region inside the P body

149 (internal FRAP) (Figure 2E and 2F). Measurements revealed considerable recovery

150 that progresses from the periphery to the center of the P body (Figure S2A). Despite

151 exhibiting a higher mobile fraction than whole FRAP, the rate of recovery (Figure S2B)

152 indicates that Me31B exchanges slower internally compared to liquid-like

153 condensates. Overall, these data show that P bodies in the mature oocyte adopt a

154 less dynamic and arrested physical state.

155 **Weak intermolecular, cytoskeletal and RNA interactions regulate P physical**

156 **properties**

157 Previous work has shown that activation of the mature oocyte results in an influx of

158 monovalent and divalent ions, release of stored mRNAs, and reorganization of the

159 actin cytoskeleton (Kaneuchi *et al.*, 2015; York-andersen *et al.*, 2015; Andersen *et al.*,

160 2020). We therefore wondered if these factors could regulate the physical properties

161 of P bodies in the mature oocyte, prior to egg activation.

162 Various molecular interactions have been shown to contribute to RNP condensation

163 including electrostatic, cation-pi and hydrophobic interactions (Kato *et al.*, 2012;

164 Brangwynne, Tompa and Pappu, 2015; Nott *et al.*, 2015; Pak *et al.*, 2016; Riback *et*

165 *al.*, 2017; Murthy *et al.*, 2019; Dzuricky *et al.*, 2020). The interactions that are thought

166 to drive the assembly of P bodies can be interpreted through the lens of a pseudo-two

167 component phase diagram (Figure 3A). In particular, by changing the solution

168 conditions to weaken the interactions that contribute to P body assembly, theory and

169 simulations predict an increase in internal mobility and more spherical condensates,

170 as shown previously for protein-RNA condensates (Boeynaems *et al.*, 2019).

171 To test if hydrophobic interactions are required for *in vivo* P body integrity, we treated
172 mature oocytes with the aliphatic alcohol 1,6-hexanediol (1,6-HD), a compound
173 identified originally in the context of attenuating hydrophobic interactions (Ribbeck and
174 Go, 2002; Patel *et al.*, 2007). Addition of 1,6-HD resulted in the transformation of P
175 bodies from irregular to spherical morphologies and an increase in condensate fusion
176 events (Figure 3B, 3C, and S3A). These results support a model in which 1,6-HD
177 weakens the intermolecular interactions that contribute to P body integrity. To further
178 test if the disruption of hydrophobic interactions leads to a transition from an arrested
179 to a more dynamic state, we performed whole FRAP on 1,6-HD treated P bodies.
180 Consistent with our model, 1,6-HD treated P bodies exhibit rapid and sustained
181 recovery (Figure 3D, S3B, and S3C). Taken together, our results suggest that
182 hydrophobic interactions contribute to regulating the arrested state of P bodies.

183 We next examined if electrostatic interactions contribute to P body physical properties
184 by testing the impact of monovalent (NaCl) or divalent salt ($MgCl_2$). At low
185 concentrations of NaCl, P bodies assemble into clusters while at high concentrations
186 they dissociate (Figure 3E). However, at a specific range of concentrations (300 – 600
187 mM), P bodies adopt spherical morphologies, consistent with a more dynamic state.
188 These results are supportive of a model in which electrostatic interactions, like
189 hydrophobic interactions, play a role in dictating physical properties and can be tuned
190 up or down by decreasing or increasing the monovalent salt concentrations,
191 respectively.

192 Interestingly, the addition of 20 mM $MgCl_2$ had no apparent effect on P body integrity,
193 yet a small increase to concentrations as low as 50 mM $MgCl_2$ results in their complete
194 dissociation (Figure 3E'). This relative sensitivity to divalent cations implies an effect
195 beyond simply ionic strength. Collectively these data suggest that changes in salt
196 concentration can alter P body integrity, likely via both ion-specific effects and
197 electrostatic screening. This is consistent with the morphology and state of P bodies
198 that we observe following *ex vivo* egg activation or in the early embryo (York-andersen
199 *et al.*, 2015).

200 Given the importance of electrostatic interactions, we asked if P body integrity was
201 regulated exclusively by protein-protein interactions, or if protein-RNA interactions
202 also contribute. To test this, we treated mature oocytes with RNase A, which leads to

203   P body dissociation over a time course of 30 minutes (Figure 3F). This result reveals

204   that that *in vivo* P body integrity depends, at least in part, on protein:RNA interactions

205   but this does exclude a contribution from protein-protein interactions.

206   Finally, to examine the role of actin in regulating P body integrity, mature oocytes were

207   treated with cytochalasin D, a commonly used actin depolymerizing agent. This

208   treatment resulted in the dissociation of P bodies in 30 minutes, consistent with our

209   data from *ex vivo* egg activation (Figure 3F'). Taken together, these results indicate

210   that multiple factors regulate P body integrity and morphology in the mature oocyte.

211   **IDRs regulate the physical state of Me31B condensates *in vitro***

212   Having established a role for multiple external factors in the regulation of P body

213   integrity, we next asked how the Me31B protein may be contributing to P body physical

214   state. Me31B contains an ATP-binding domain and folded helicase domain, flanked

215   by short N- and C-terminal IDRs (Figure 4A). While the function of the helicase domain

216   is well known, the function of the disordered regions is rather unclear. Since Me31B is

217   an essential *in vivo* protein, we adopted an *in vitro* approach to examine the role of

218   these disordered regions.

219   First, we tested if the purified recombinant Me31B (GFP-Me31B) can undergo phase

220   separation *in vitro*. While Me31B is diffuse at physiological protein concentrations (7.5

221   μM), upon the addition of a small amount of crowding agent (1% PEG) Me31B

222   undergoes phase separation to form condensates (Figure 4B). We reproduced Me31B

223   condensation using a secondary crowding agent (1% Ficoll), demonstrating that

224   Me31B phase separation does not result from the specific chemical properties of the

225   used crowding agent (Figure S4A). Time lapse imaging revealed that Me31B initially

226   forms condensates with highly dynamic properties, as evidenced by an increase in

227   condensate size (Figure S4B). However, over time these condensates become less

228   dynamic, as the apparent fusion kinetics of Me31B condensates slows as a function

229   of time (Figure S4C). To test whether or not the Me31B molecules in the initial

230   condensates are mobile, we performed both whole FRAP and internal FRAP on freshly

231   formed condensates. To our surprise, these showed little or no recovery after

232   photobleaching, indicating that Me31B condensates are present in an arrested

233   physical state similar to *in vivo* P bodies (Figure 4C).

234 It has been suggested that the assembly and properties of RNP condensates is

235 regulated by IDRs (Lin, David S.W. Protter, *et al.*, 2015; Martin and Mittag, 2018;

236 Martin *et al.*, 2020). Previous work has shown that the sequence length and position

237 of IDRs varied greatly between DDX6 and Dhh1 (Hondele *et al.*, 2019). To examine

238 the extent of variation across the DDX6 family of proteins, we performed a sequence

239 analysis of Me31B orthologs. This revealed that folded domains are highly conserved

240 while IDR length and sequence varied substantially (Figure 4D).

241 To better understand how the IDRs might contribute to function, we performed all-

242 atom simulations of full-length Me31B. Simulations revealed that both IDRs adopt a

243 heterogeneous ensemble of states (Figure 4E). Interestingly, both N- and C- terminal

244 IDRs interacted transiently and relatively non-specifically with the surface of the folded

245 domains. These contacts were mediated through electrostatic and hydrophobic

246 interactions (Figure 4F, S4D, and S4E). Rather than acting as drivers of self-assembly,

247 our simulations suggest the possibility that IDRs play a modulatory role.

248 To test for the modulatory influence of IDRs in Me31B phase separation, we next

249 purified recombinant Me31B with both IDRs deleted (Me31BΔN-ΔC). Consistent with

250 the interpretation from our simulations, Me31BΔN-ΔC rapidly self-assembled into

251 solid-like aggregates (Figure 4F and S4F). These results demonstrate that protein-

252 protein interactions can be established independently of the IDRs and suggests that

253 the folded domain plays an important role in driving self-assembly. Importantly, our

254 results demonstrate that the IDRs tune the physical properties of Me31B condensates,

255 attenuating the strong interactions established among the interacting folded domains.

256 Taken together, our results show that recombinant Me31B is prone to form

257 condensates with a less dynamic and arrested physical state, consistent with *in vivo*

258 data. Importantly, the short IDRs from Me31B function to modulate the condensate

259 physical state, suggesting that the interactions that drive Me31B self-assembly

260 originate from the folded domains.

261 **Tral is key to regulating organization of P bodies in the mature oocyte**

262 In addition to Me31B, several other proteins localize to, or are found to be enriched

263 within P bodies (Lin *et al.*, 2008). Given the importance of disordered regions within

264 Me31B, we hypothesized that intrinsically disordered proteins (IDPs) within P bodies

265   could potentially act as lubricants to regulate P body assembly and organization

266   through interactions with structured proteins. To test this, we first performed disorder

267   prediction across the set of known P body proteins to estimate the proportion of

268   structured versus disordered regions (Figure 5A). Approximately 50% of proteins

269   known to localize to P bodies in *Drosophila* contain long IDRs, highlighting the

270   structural heterogeneity of components within P bodies. Among the proteins enriched

271   with intrinsic disorder is Tral, a member of the LSM protein family (RAP55 in

272   vertebrates, CAR-1 in *C. elegans*). Additionally, Tral is also known to interact directly

273   with Me31B, function in *Drosophila* axis patterning (Bouveret, 2000; Monzo *et al.*,

274   2006; Tritschler *et al.*, 2007, 2008, 2009; Götze *et al.*, 2017; Wang *et al.*, 2017; Hara

275   *et al.*, 2018; McCambridge *et al.*, 2020) and is predicted to be largely disordered with

276   the exception of an N-terminal LSM domain (Figure 5B).

277   We therefore tested the role of Tral in the regulation of P body assembly *in vivo*. In

278   mature oocytes expressing GFP::Tral, like Me31B, Tral associates with P body

279   condensates (Figure 5C). Despite being localized to the same condensate, different

280   proteins do not need to follow equivalent dynamics (Boeynaems *et al.*, 2019). We

281   therefore asked whether Tral shows similar *in vivo* behaviors to Me31B, which would

282   suggest that these two proteins are associated with the same physical state. Indeed,

283   despite being structurally distinct from Me31B, whole FRAP and 1,6-HD experiments

284   on Tral were consistent with our results for Me31B (Figure 5D). This supports a model

285   in which Me31B and Tral are strongly coupled within P bodies, likely through direct

286   interaction or interaction with a common intermediate (e.g., RNA).

287   Work in arrested *C. elegans* oocytes has shown that the organization and properties

288   of germline P bodies is regulated by orthologs of Tral (CAR-1) and Me31B (CHG-1),

289   where loss of CGH-1 resulted in the formation of morphologically deformed P bodies

290   with altered physical properties (Hubstenberger *et al.*, 2013). Since Me31B is essential

291   for *Drosophila* oogenesis, we tested if Tral is required to regulate Me31B labeled P

292   bodies in the mature oocyte. Remarkably, in Tral mutants, P bodies have dramatically

293   different morphologies and form rod and planar donut-shaped assemblies (Figure 5E),

294   implying a gain of anisotropy in the underlying molecular arrangement of the

295   condensate. The formation of apparently ordered (or partially ordered) assemblies is

296   reminiscent of liquid-crystalline formation as observed in the synaptonemal complex

297 or in specific mutants of the plant protein FLOE1 (Rog, Köhler and Dernburg, 2017;

298 Dorone *et al.*, 2020). These results suggest that despite being structurally distinct, Tral

299 and Me31B contribute to the assembly and organization of P bodies likely through

300 synergistic interactions.

301 **The condensed and arrested state of P bodies regulate *bcd* mRNA**

302 Our data shows that P bodies in the mature *Drosophila* oocyte are present in a less

303 dynamic, arrested physical state. This is in contrast to previous data in cells where

304 related RNP condensates are shown to exhibit dynamic behavior adopting liquid-like

305 states (Kroschwald *et al.*, 2015). Since P bodies in the mature oocyte contain maternal

306 mRNAs that are stored and translationally regulated over long periods, we

307 hypothesized that the less dynamic and arrested physical state could be required for

308 this function.

309 The anterior determinant *bcd* mRNA is a well-established example of long-term

310 storage and localizes to P bodies in the mature oocyte (Figure 6A). To address if the

311 condensed state of P bodies is required for the association with *bcd* mRNA, we first

312 tested the change in P body and *bcd* mRNA distribution following egg activation. Using

313 a previously established *ex vivo* egg activation assay, we show that both P bodies and

314 *bcd* mRNA undergo rapid dispersion (Figure 6B). This result indicates that the

315 transition of P bodies from a condensed to diffused state leads to the release of *bcd*

316 mRNA. This finding is consistent with data arguing that translation of *bcd* mRNA only

317 occurs after egg activation and when the mRNA is no longer inside of P bodies (Weil

318 *et al.*, 2012; Eichhorn *et al.*, 2016).

319 To further explore this phenomenon, we developed a simple coarse-grained model in

320 which protein and RNA will co-assemble to form condensates *in silico* (Figure 6C and

321 S5). In our model, protein and RNA molecules possess attractive protein:protein and

322 protein:RNA interactions that form multi-component condensates through phase

323 separation. Condensate stability depends on both the strength of protein-protein and

324 protein-RNA interactions, such that over the concentration range examined both

325 species are necessary for phase separation. In simulations where the protein-protein

326 interaction strength is systematically weakened we observe a concomitant release of

327 RNA into the dilute phase and loss of condensate integrity. These simulations predict

328   that condensate integrity can be viewed as a proxy for RNA sequestration and storage.

329   We therefore sought to test this prediction *in vivo*.

330   Since we can experimentally alter the physical state of P bodies with small molecules,

331   we asked if an arrested state is necessary for the association of *bcd* mRNA with P

332   bodies. Upon 1,6-HD treatment of mature oocytes, both P bodies and *bcd* mRNA

333   initially adopt spherical morphologies, consistent with a loss of P body integrity and

334   transition to a more dynamic state (Figure 6D). However, in line with our predictions,

335   while P bodies remain condensed and spherical, *bcd* mRNA becomes diffuse and is

336   no longer observed in P bodies (Figure 6E and 6F). Together, these data suggest that

337   changing the state of P bodies, either experimentally or with a developmental cue,

338   causes release and potentially translation of stored mRNAs.

DISCUSSION

Over the last decade, biomolecular condensates have emerged as a key principle in cellular organization. While changes in condensate physical properties have been examined extensively *in vitro*, the *in vivo* importance and function of physical states has been much less explored. In this study, we focused on the physical properties that are likely to enable P bodies to regulate mRNA in mature *Drosophila* oocytes. We demonstrate that a combination of intrinsic (intermolecular interactions, presence of IDRs) and extrinsic (RNA, actin, disordered proteins) factors can regulate the integrity and the arrested physical state of P bodies, both of which allow regulation of *bcd* mRNA *in vivo*. Overall, we propose that condensates with less dynamic, arrested physical states offer a controlled mechanism for long-term storage of translationally repressed mRNAs.

While dynamic, liquid-like states have been observed for many biomolecular condensates, there is a growing repertoire of functionally important and dynamically arrested condensates (Brangwynne, Mitchison and Hyman, 2011; Hubstenberger *et al.*, 2013; Boke *et al.*, 2016; Woodruff *et al.*, 2017). Balbiani bodies, for instance, adopt a solid-like physical state which is thought to facilitate prolonged storage of organelles and macromolecules in dormant vertebrate oocytes (Boke *et al.*, 2016). Similarly, the nucleolus in *Xenopus laevis* oocytes is shown to exist in a highly viscous physical state under physiological conditions (Brangwynne, Mitchison and Hyman, 2011). P bodies in *Drosophila* eggs also exhibit a similar physical state which likely enables long term storage of maternal mRNAs by strongly inhibiting access to ribosomes in the cytoplasm. Analogous properties have been observed in the germline P bodies of arrested *C. elegans* oocytes (Hubstenberger *et al.*, 2013), suggesting that less dynamic and arrested properties of RNP condensates could be an evolutionarily conserved mechanism to temporally regulate mRNAs essential for normal development. Importantly, dynamically arrested physical states of RNP condensates are likely not limited to egg cells but may be preserved across other specialized cell types such as neurons. For example, mRNAs stored and translationally repressed in neuronal RNP condensates are temporally translated in an activity induced manner at specific synapses, thereby influencing short-term or long-term memory (Rajasethupathy *et al.*, 2009; Puthanveettil, 2013). While it is not clear how this translation is regulated, models suggest that RNP granules switch between dynamic

372 liquid-like and solid-like states to facilitate differential translation control (Majumdar *et al.*, 2012; Sudhakaran and Ramaswami, 2017; Bakthavachalu *et al.*, 2018). Beyond RNPs, in *A. thaliana,* dynamically arrested cytoplasmic condensates rewire transcription by sequestering a subset of the auxin-responsive transcription factor, preventing its nuclear function (Powers *et al.*, 2019)*.*

377 One striking observation is the influence of disordered regions and/or proteins in regulating the physical state of P body condensates. Conventional wisdom posits that IDRs contribute weak multivalent interactions that are essential for phase separation. In support of this model, many proteins that undergo phase separation contain IDRs that are necessary and sufficient for assembly (Lin, David S.W. Protter, *et al.*, 2015; Protter *et al.*, 2018). Our results offer an alternative model; rather than driving assembly, IDRs may also function to modulate and tune interactions between folded domains, potentially providing a local lubricant that counteracts strong multivalent interactions driven by adhesive interaction sites on folded domains. In the absence of IDRs, the folded domains from Me31B undergo irreversible aggregation. As such, the IDRs provide evolutionarily malleable modules to tune the physical state of condensates. This model echoes prior work on the yeast prion protein Sup35, where the loss of N-terminal disordered regions lead to robust aggregation of the folded C-terminal domain, while the full-length protein rapidly assembles into dynamic condensates that rapidly mature into gel-like assemblies (Franzmann *et al.*, 2018). As such, we speculate that the disordered regions across Me31B orthologs (and indeed more generally DDX helicases) may have emerged to modulate the physical state of the resulting RNP complexes that form, be they micron-scale membrane-less organelles such as P bodies, or mesoscopic clusters of protein and RNA.

396 One other key determinant that regulates biomolecular condensates is multivalency. Condensates such as P bodies contain hundreds of diverse RNP components which serve as a major source of multivalent interactions that control their integrity and physical properties. While structured and disordered RNA-binding proteins have been investigated previously whether or how they influence the overall property of condensates *in vivo*, was unclear. Using Me31B and Tral, our data indicates that structurally distinct proteins synergistically interact to regulate the assembly and organization of P bodies during *Drosophila* oogenesis. Despite being structurally

404   different to Me31B, Tral exhibits strikingly similar physical properties as Me31B when
405   examined in P body condensates. However, loss of Tral results in structurally
406   deformed and physically altered P bodies. These data also agree with observations
407   reported for Tral and Me31B orthologues in arrested *C. elegans* oocytes
408   (Hubstenberger *et al.,* 2013) suggesting that despite sequence and structural
409   divergence, the underlying molecular and physical interactions between components
410   of RNP condensates may be evolutionarily conserved.

411   Prior to this work, it was unclear how stored mRNAs could be subjected to differential
412   release and translation at distinct developmental stages without obviously disrupting
413   the integrity of P bodies. As demonstrated for several RNA binding proteins, the
414   assembly and physical properties of RNP condensates are largely regulated by weak
415   intermolecular forces. We show that the physical properties of P bodies in the mature
416   oocyte are disrupted by both 1,6-HD and salt, implicating a role for hydrophobic and
417   electrostatic interactions in P body integrity. We speculate that modulating the
418   strengths of different interactions allows P bodies to adjust their physical state, thereby
419   facilitating fine-tuned control of mRNA storage and subsequent translation in response
420   to developmental cues.

421   In summary, we describe the less dynamic, arrested physical state of Me31B labeled
422   P body condensates and their potential role in regulating the storage of *bcd* mRNA in
423   the mature *Drosophila* oocyte. The ability of weak intermolecular interactions, modular
424   protein regions and cellular factors to regulate condensate physical state provides an
425   elegant mechanism for P bodies to respond to cellular and developmental cues (Figure
426   7). We predict that such physical states are likely a universal feature of RNP
427   condensates in specialized cells that require long term translational regulation of
428   stored mRNAs.
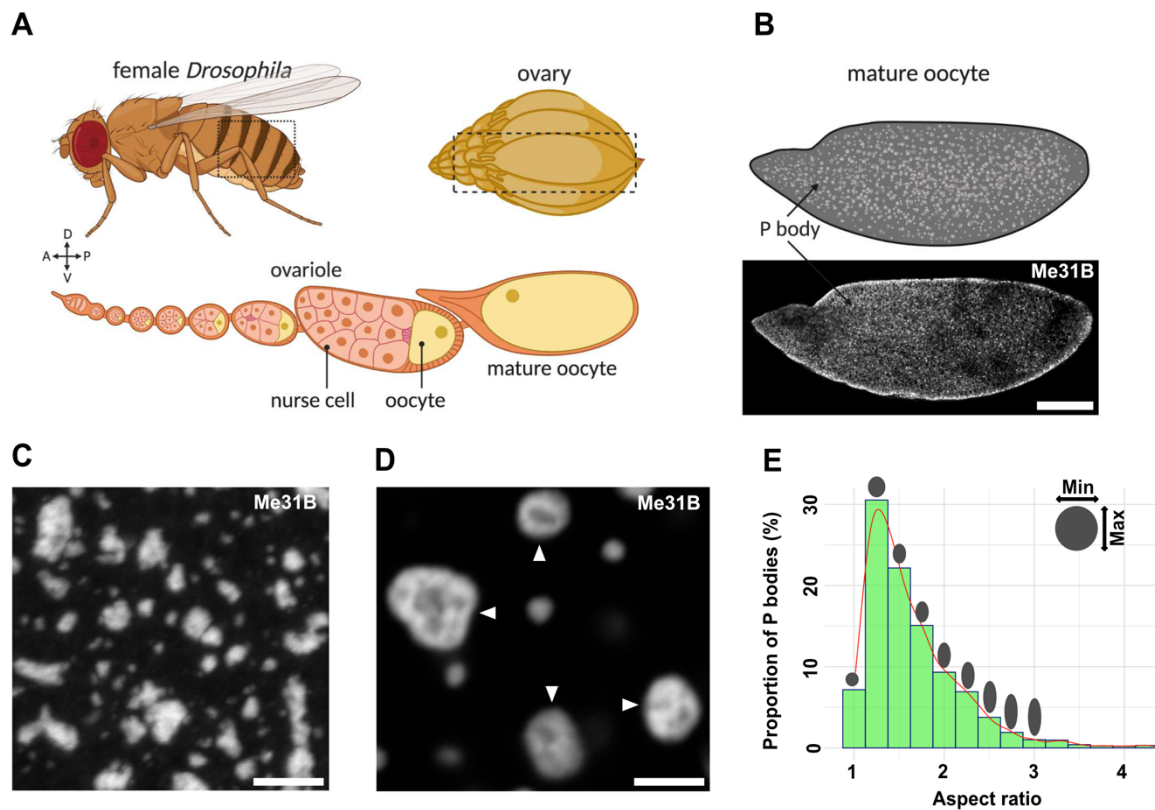
FIGURE 1

Figure 1: Me31B forms heterogeneous P body condensates in the mature oocyte

(A) Schematic of a *Drosophila* female, ovary and ovariole. Each female contains two ovaries that are each comprised of 16-18 ovarioles. Each ovariole can be thought of as an assembly line for the production of mature oocytes. The oocyte is supported by a collection of nurse cells until the late stages of oogenesis. Created with BioRender.com

(B-E) Mature oocyte expressing Me31B::GFP.

(B) Cartoon depicting P body distribution in the mature oocyte and confocal image of a whole mature oocyte showing P bodies throughout the cytoplasm. The concentration of P bodies at the cortex is in part due to this being a cross section image.

(C) Increased magnification reveals P bodies exhibit diverse morphologies and sizes. Maximum projection 10 μm.

(D) Representative image of P bodies exhibiting multiple subdomains (white arrowheads) indicative of heterogeneous internal organization.

(E) Aspect ratio analysis of individual P bodies (>1 μm) showing an uneven range of P body morphology.

Scale bar = 100 μm (B), 5 μm (C,D).

447 **FIGURE 2**
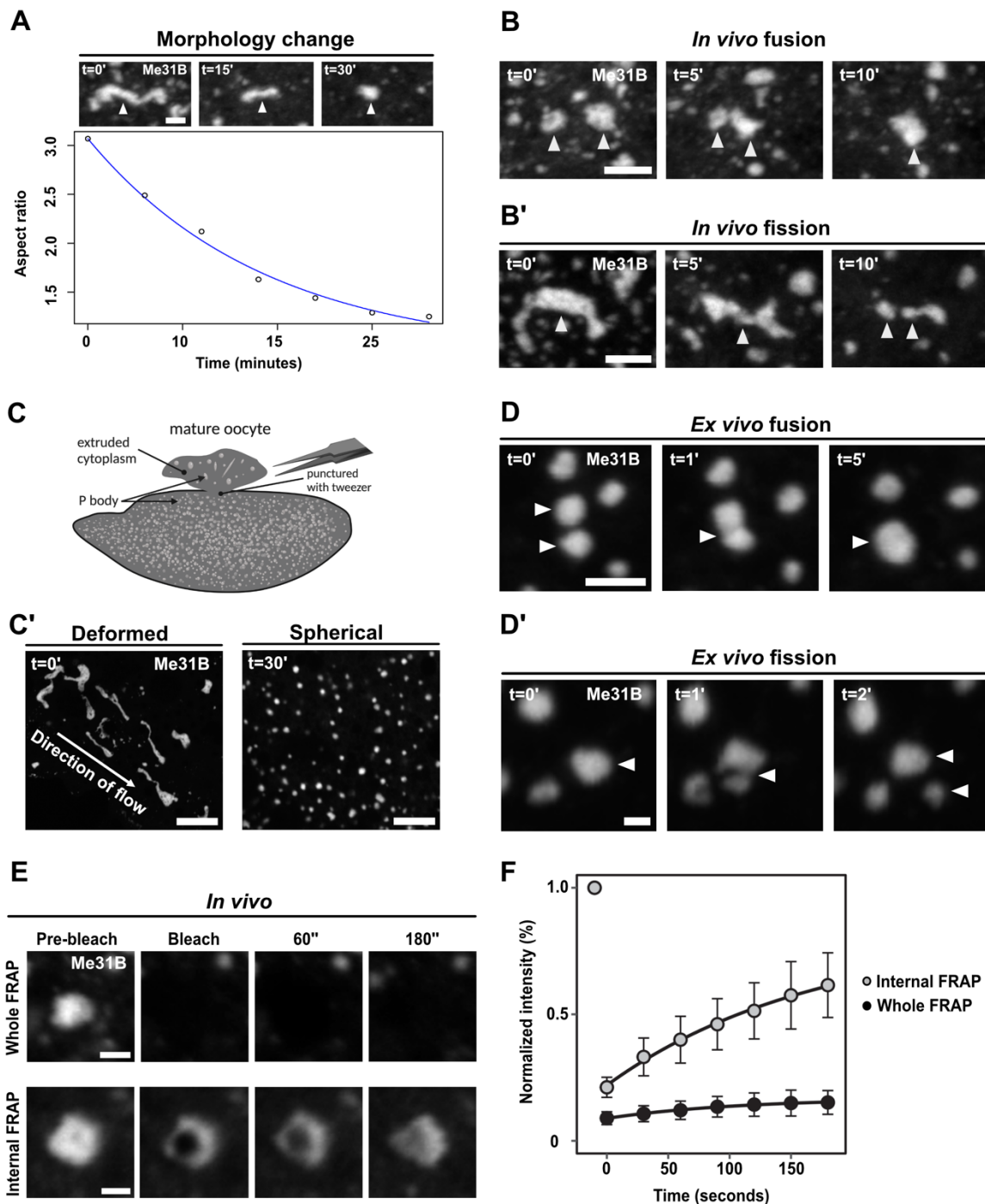
448 **Figure 2: P bodies adopt a less dynamic and arrested physical state**

449 **(A, B, B', C', D, D', E)** Mature oocyte expressing Me31B::GFP.

450 **(A)** Time series of a P body displaying elastic behaviour, starting in an extended state

451 (t=0') and subsequently relaxing towards a spherical morphology (t=30'). Plot of

452 individual P body (n = 10) A.R over time showing relaxation from extended (A.R~3) to

453 spherical morphology (A.R~1).

454 **(B)** Time series of two *in vivo* P bodies undergoing coalescence (white arrowheads).

455 (**B'**) Time series of a single *in vivo* P body undergoing fission to form two distinct

456 condensates (white arrowheads).

457 **(C)** Cartoon depicting cytoplasmic extrusion of P bodies into halocarbon oil (*ex vivo*)

458 induced by puncturing the outer membrane of the mature oocyte. Created with

459 BioRender.com **(C')** Confocal image of *ex vivo* P bodies displaying stretched elastic

460 morphologies shortly after extrusion (t=0'). Over time, extruded P bodies relax into

461 homogeneous spherical condensates (t=30').

462 **(D)** Time series of *ex vivo* P bodies undergoing coalescence (white arrowheads). **(D')**

463 Time series of *ex vivo* extruded P bodies undergoing fission (white arrowheads).

464 **(E)** Time series of whole FRAP of P body shows minimal recovery, while internal FRAP

465 of P body shows increased recovery of Me31B fluorescence.

466 **(F)** P body recovery profiles after whole FRAP and internal FRAP (n = 20 P bodies for

467 whole FRAP and n = 24 P bodies for internal FRAP).

468 Scale bar = 2.5 µm (A), 5 µm (B,B',D,D'), 10 µm (C'), 1.5 µm (E).

469 **FIGURE 3**
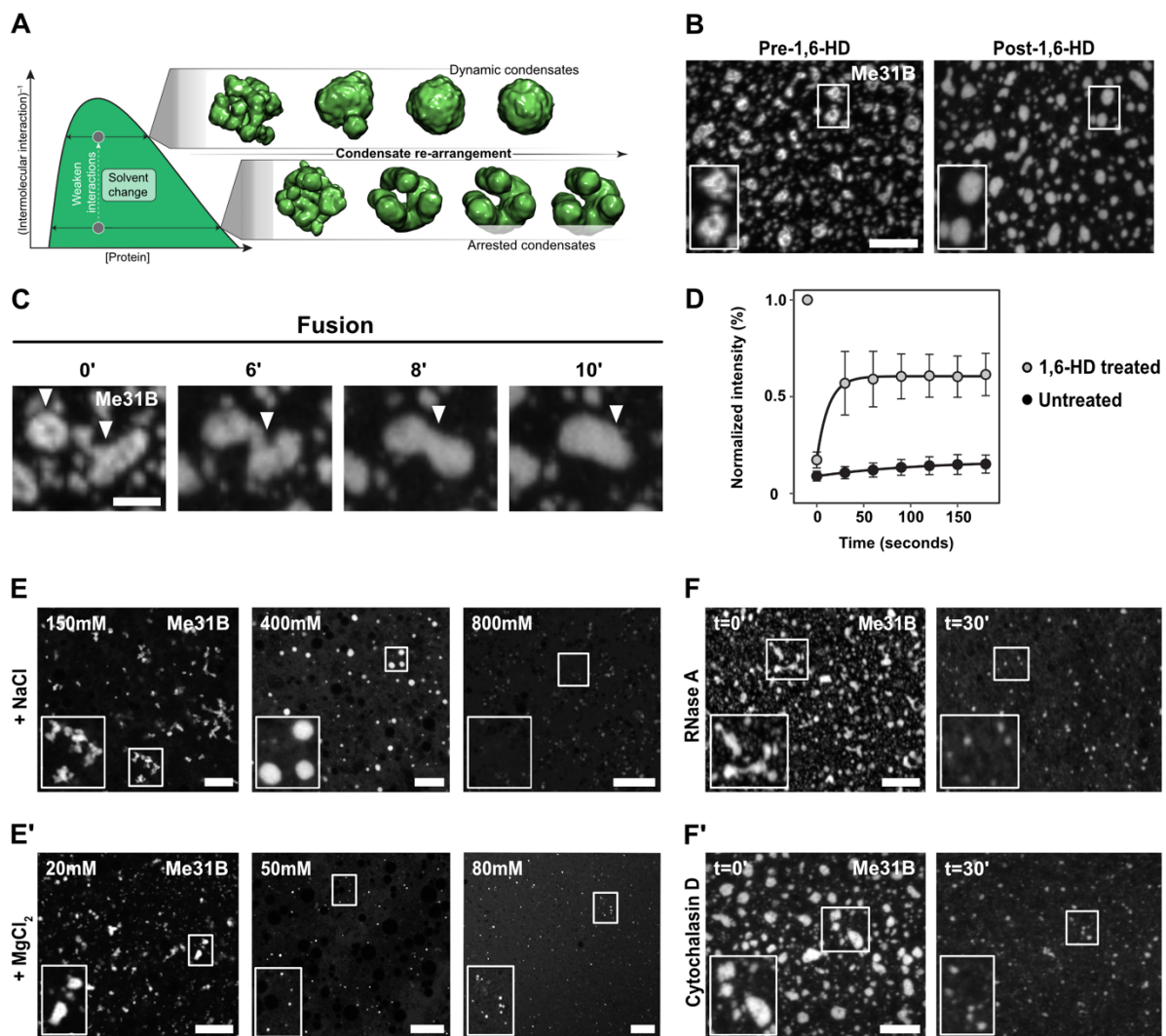
470 **Figure 3: P body physical properties are regulated by hydrophobic and**
471 **electrostatic interactions along with RNA and actin**

472 **(A)** Schematized phase diagram in which protein concentration extends along the x-
473 axis whereas molecular interaction strength extends across the y-axis. Inset shows
474 snapshots from coarse-grained simulations performed at distinct position along the y-
475 axis. Condensate morphology is dependent on intramolecular interaction strength,
476 such that weak intermolecular interactions lead to spherical condensates, while strong
477 intermolecular interactions lead to kinetically arrested amorphous condensates.

478 **(B,C,E-F')** Mature oocyte expressing Me31B::GFP.

479 **(B)** Addition of 5% 1,6-HD causes P bodies to transform from amorphous to spherical
480 morphology. Furthermore, addition of 1,6-HD results in the loss of internal
481 heterogeneity of P bodies. Maximum projection 5 μm.

482   **(C)** Time series shows two P bodies undergoing coalescence following the addition of

483   1,6-HD. Maximum projection 5 µm.

484   **(D)** Whole FRAP recovery profile of 1,6-HD treated P bodies (n = 12) showing rapid

485   fluorescence recovery compared to untreated P bodies (n = 24).

486   **(E)** Addition of varying concentrations of NaCl results in diverse physical states of

487   extruded P bodies ranging from sticky (150 mM) to liquid-like (400 mM) and diffuse

488   state (800 mM). **(E')** Treatment with $MgCl_2$ results in the dissociation of extruded P

489   bodies at concentrations significantly lower than NaCl.

490   **(F)** Treatment with 500 ng/µl RNase A (degrades RNA) or **(F')** 10 µg/µl cytochalasin-

491   D (depolymerizes actin) causes P body dissociation, resulting in smaller condensates.

492   Maximum projection 10 µm.

493   Scale bar = 5 µm (B,C,E,E',F,F')

494   **FIGURE 4**
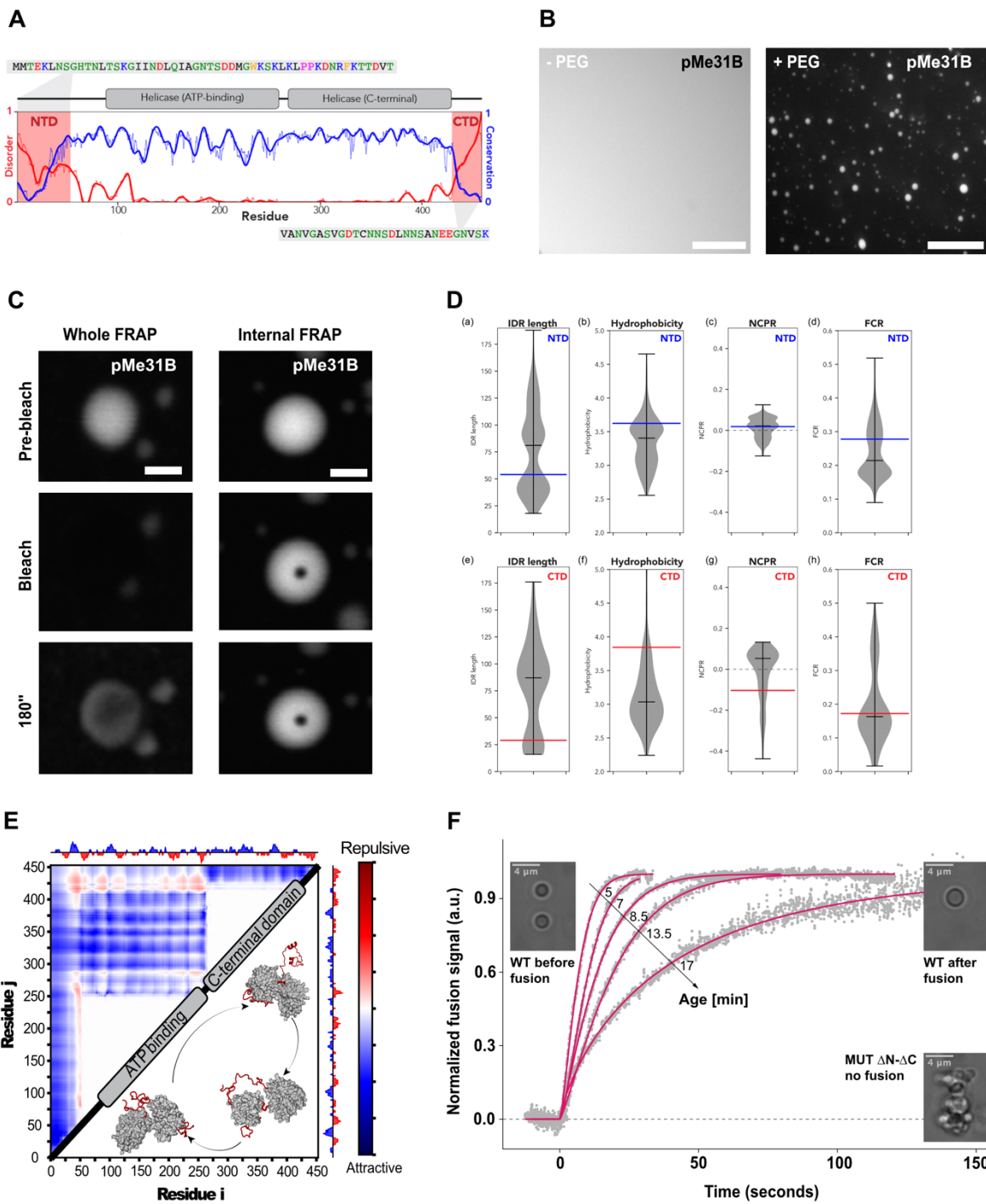
495   **Figure 4: Deletion of IDRs results in the aggregation of Me31B condensates *in***

496   ***vitro***

497   **(A)** Purified GFP-Me31B (pMe31B) at 7.5 µM is diffuse on its own, but forms phase

498   separated spherical condensates in the presence of 1% PEG. Maximum projection 5

499   µm.

500 **(B)** Time series of pMe31B condensates subjected to FRAP experiments. Whole P

501 body photobleaching shows moderate fluorescence recovery, while internal FRAP

502 shows no recovery.

503 **(C)** Violin plots quantify density of IDR length (a/e), hydrophobicity (b/f), Net charge

504 per residue (c/g) and fraction of charged residues (d/h) for the N-terminal IDRs (a-d)

505 or C-terminal IDRs (e-h). Blue or red bars define the associated value for the Me31B

506 IDR in the N- or C-terminal IDR, respectively.

507 **(D)** Overview of disordered, conservation, and domain architecture for Me31B.

508 Conservation calculated across 566 orthologous sequences. CTD and NTD

509 sequences are highlighted, with an atomistic model of the full-length protein shown

510 below.

511 **(E)** Summary of all-atom simulations. Normalized inter-residue distance is shown, with

512 cooler colors reflecting attractive interactions and warmer colors reflecting repulsive

513 interactions. Normalized distances are calculated based on the expected distance for

514 a self-avoid polymer model. Both the NTD and CTD engage directly with the folded

515 domains in a distributed and transient manner. Interactions are relatively uniform

516 across the folded domain surface.

517 **(F)** Fusion of pMe31B condensates (magenta) at different time points post

518 condensation, quantified by dual-trap optical tweezers. pMe31B ΔN-ΔC condensates

519 (dashed line) do not fuse and rapidly aggregate with each other.

520 Scale bar = 5µm (A,F), 2.5µm (B).

521   **FIGURE 5**
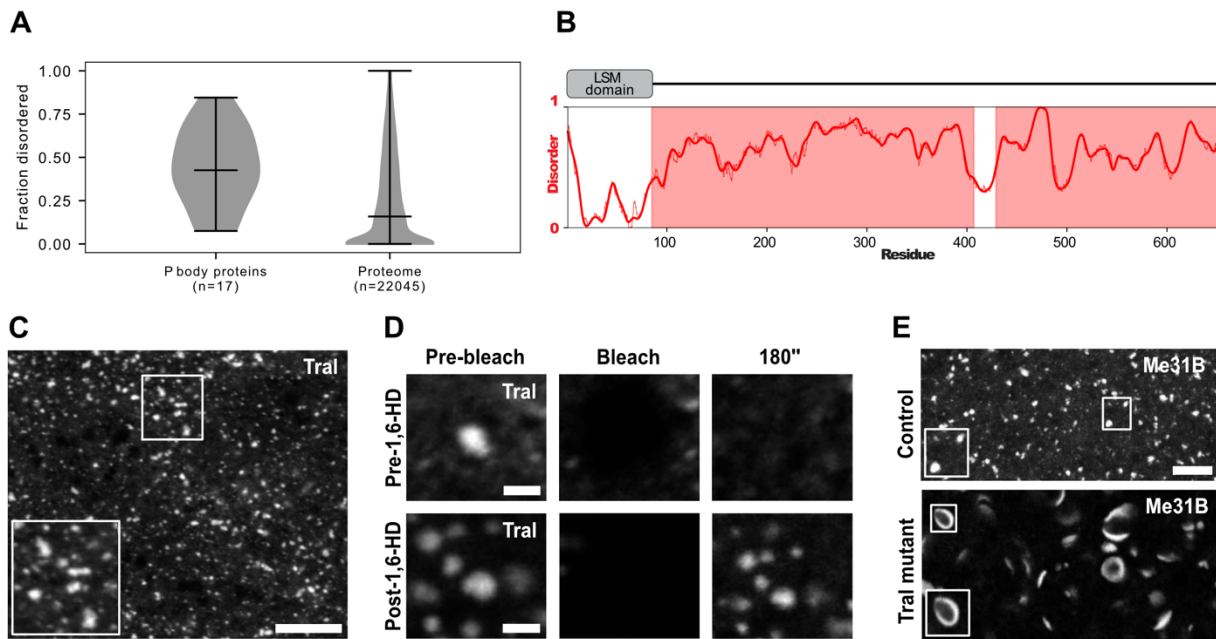
522   **Figure 5: Absence of Tral alters P body morphology in the mature oocyte**

523   **(A)** Comparison of fraction disorder in known *Drosophila* P body proteins (left)

524   compared to whole *Drosophila* proteome (right).

525   **(B)** Schematic of Tral domain architecture containing a structured LSM domain

526   followed by a long stretch of highly disordered regions.
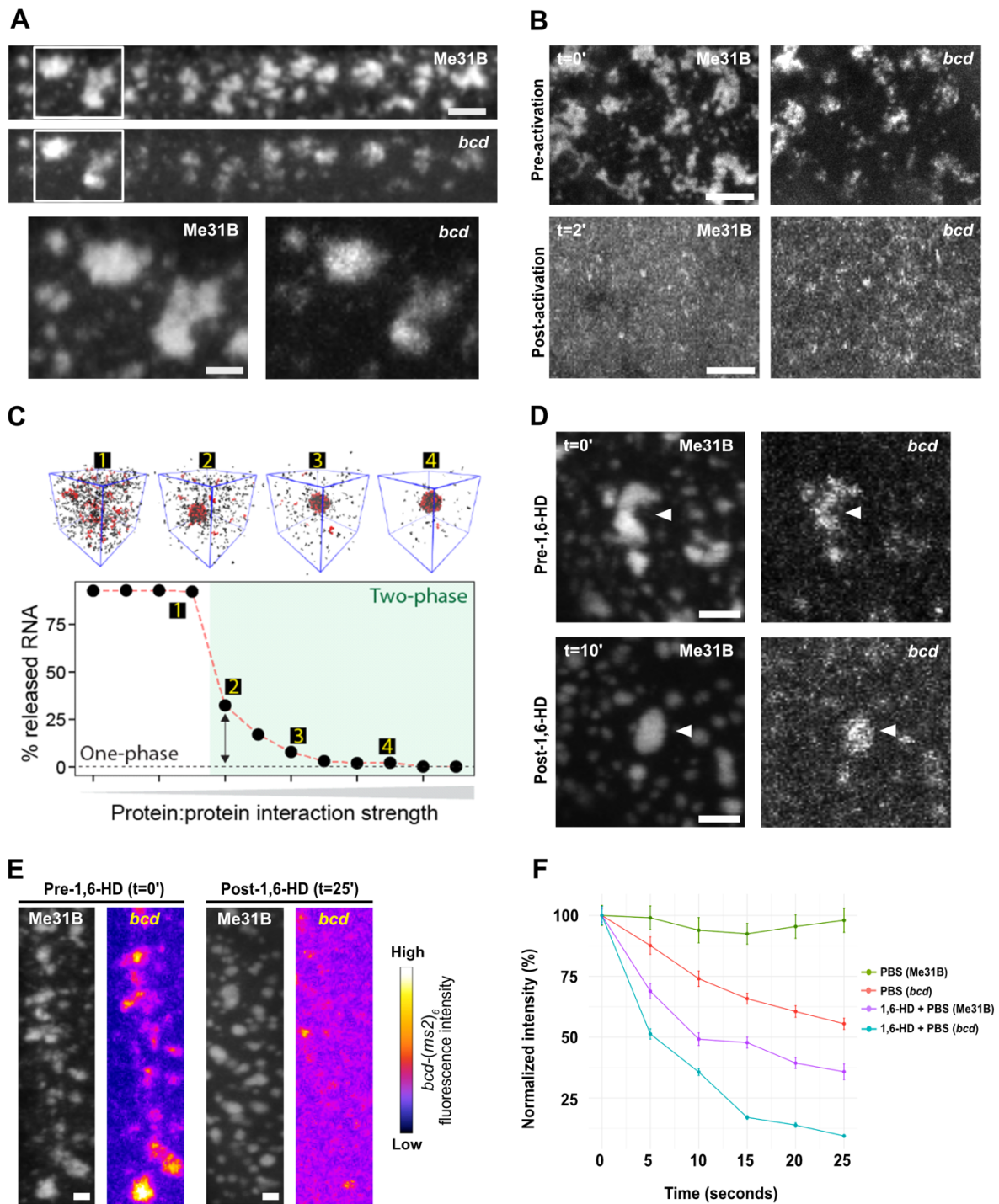
527   **(C,D)** Mature oocyte expressing GFP::Tral.

528   **(C)** Tral localizes to P body condensates with diverse morphologies and sizes,

529   distributed throughout the oocyte cytoplasm. Maximum projection 7 μm.

530   **(D)** Time series of FRAP experiments on GFP::Tral condensates before and after

531   treatment with 1,6-HD. Prior to the addition of 1,6-HD, Tral condensates do not recover

532   after photobleaching, however, Tral condensates treated with 1,6-HD show increased

533   fluorescence recovery post photobleaching.

534   **(E)** Representative mature oocytes expressing Me31B::GFP, control (*tral^1* / + or

535   *Df(3L)ED4483 / +*) displaying close to spherical P body condensates. In the absence

536   of Tral (*tral^1 / Df(3L)ED4483*), Me31B forms aberrant rod and doughnut shaped P body

537   condensates. Maximum projection 5 μm.

538   Scale bar = 5μm (C,E), 1.5μm (D).

23

539 **FIGURE 6**

540 **Figure 6: Altering P body physical state leads to premature loss of *bcd* **

541 **association with P bodies**

542 **(A,B,D,E)** Mature oocyte expressing Me31B::GFP, *hsp83-MCP-RFP* and *bcd*-(*ms2*)$_6$.

543 **(A)** High resolution image of *bcd* mRNA co-localizing with P bodies at the anterior

544 region of the mature oocyte. Inset shows a zoomed in version of *bcd* mRNA and P

545 body association. Maximum projection 5 μm.

24

546 **(B)** Upon addition of activation buffer, P bodies and *bcd* mRNA simultaneously

547 undergo dispersion from condensed (t=0') to diffused state (t=2'). Maximum projection

548 5 μm.

549 **(C)** Coarse-grained simulations performed with 50 RNA molecules 800 protein

550 molecules in which condensate assembly is driven by both protein:protein and

551 protein:RNA interactions. When condensates have formed, the fraction of free (dilute

552 phase) RNA is determined by both protein:protein and protein:RNA interaction

553 strength.

554 **(D)** Addition of 1,6-HD causes P bodies and *bcd* mRNA to initially adopt a spherical

555 morphology (t=10'), representative of a more dynamic physical state. Maximum

556 projection 5 μm.

557 **(E)** Extended exposure to 1,6-HD results in dispersion of *bcd* mRNAs whereas P

558 bodies remain condensed (t=25'). Maximum projection 5 μm.

559 **(F)** Quantification of P body and *bcd* mRNA fluorescence in the presence of PBS (n =

560 37 Me31B and *bcd* particles) or 1,6-HD (n = 71 Me31B and *bcd* particles).

561 Scale bar = 2.5μm (A), 5μm (B,D), 2μm (E).

562 **FIGURE 7**
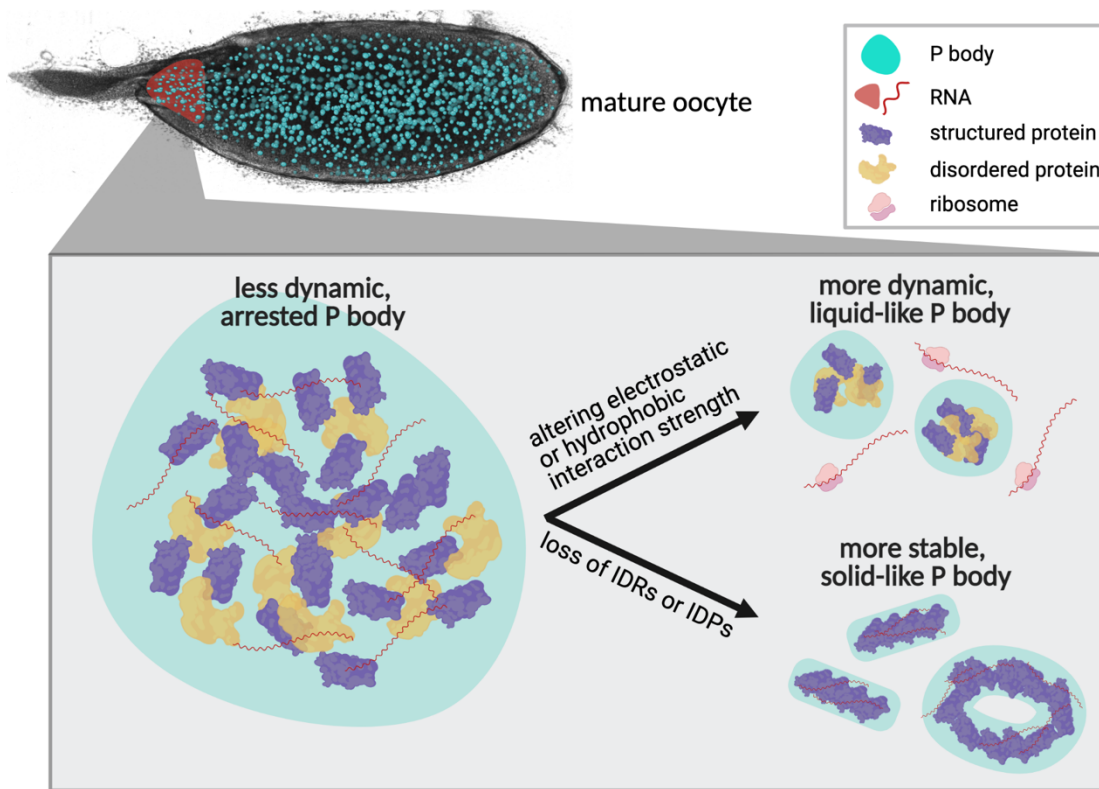
563 **Figure 7: Regulation of P bodies in the mature *Drosophila* oocyte**

564 P bodies (cyan) distributed throughout the mature *Drosophila* oocyte adopt a less

565 dynamic, arrested physical state. The assembly, organization and physical properties

566 of P bodies are regulated by synergistic interactions between structured (purple) and

567 disordered proteins (yellow), as well as RNAs, predominantly via weak intermolecular

568 hydrophobic and electrostatic interactions. Altering the strength of these interactions

569 can lead to more dynamic, liquid-like P bodies and result in the release, and

570 subsequent translation, of stored mRNAs (red). Alternatively, loss of IDRs or IDPs

571 results in the formation of morphologically aberrant, solid-like protein-RNA aggregates

572 which likely interfere with mRNA storage and translational regulation. Created with

573 BioRender.com
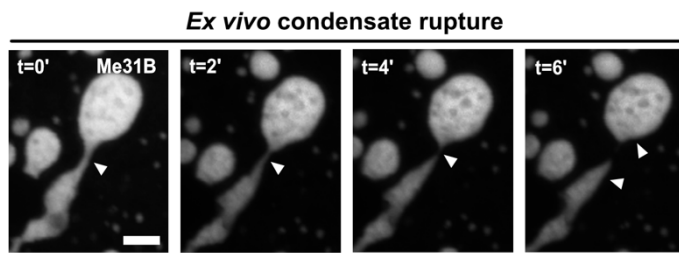
FIGURE S1

Figure S1: Extruded P bodies display rupture behavior

Time series of P bodies extruded from the mature oocyte are first held together by a transient 'bridge' after fusion. The P bodies then undergo a process of 'pinching off' of the bridge (white arrowheads point to the region of rupture). The two P bodies resorb within a minute of bridge rupturing. Scale bar: 5μm.
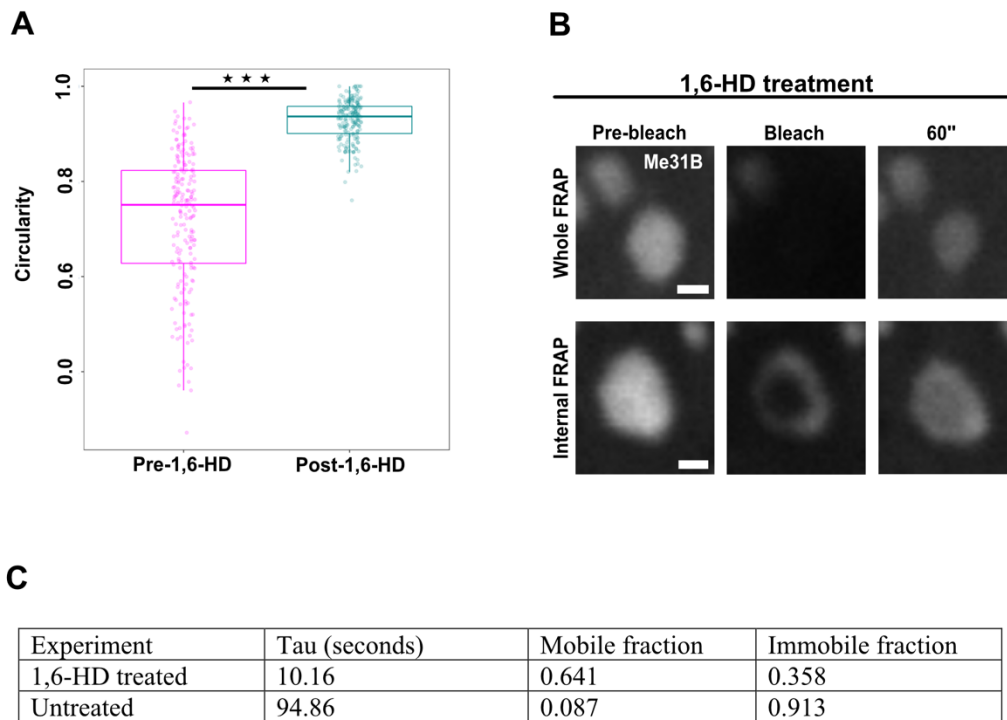
580 **FIGURE S2**

A
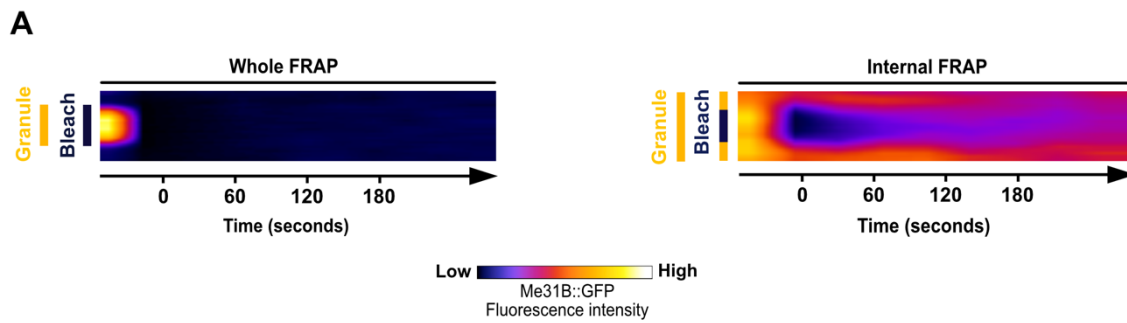
B

Experiment	Tau (seconds)	Mobile fraction	Immobile fraction
Whole FRAP	94.86	0.087	0.913
Internal FRAP	144.12	0.714	0.285

581 **Figure S2: Me31B is mobile within P bodies but not between the cytoplasm and**

582 **P bodies**

583 **(A)** Kymograph of P body whole FRAP shows no recovery, while kymograph of P

584 bodies post-internal FRAP displays recovery from the periphery to the center. This

585 pattern is indicative of diffusion mediated recovery.

586 **(B)** The tau, mobile and immobile fractions of Me31B after whole FRAP and internal

587 FRAP experiment. These data show that Me31B is more mobile internally than

588 between the P body and cytoplasm.

28

FIGURE S3

A

B

C

Experiment	Tau (seconds)	Mobile fraction	Immobile fraction
1,6-HD treated	10.16	0.641	0.358
Untreated	94.86	0.087	0.913

Figure S3: 1,6-HD induces transition of P bodies to a more dynamic physical state

(A) Quantification of P body circularity before and after 1,6-HD treatment shows a significant increase in spherical morphology of P body post-treatment (Wilcoxon signed-rank test, n = 200).

(B) Time series of P body condensates subjected to whole or internal FRAP post 1,6-HD treatment, both displaying rapid fluorescence recovery (n = 12 whole FRAP, n = 3 internal FRAP.) Scale bar: 3µm.

(C) The tau, mobile and immobile fractions of Me31B after whole FRAP with or without the addition of 1,6-HD. These data show that Me31B is highly mobile between the P body and cytoplasm post-treatment.
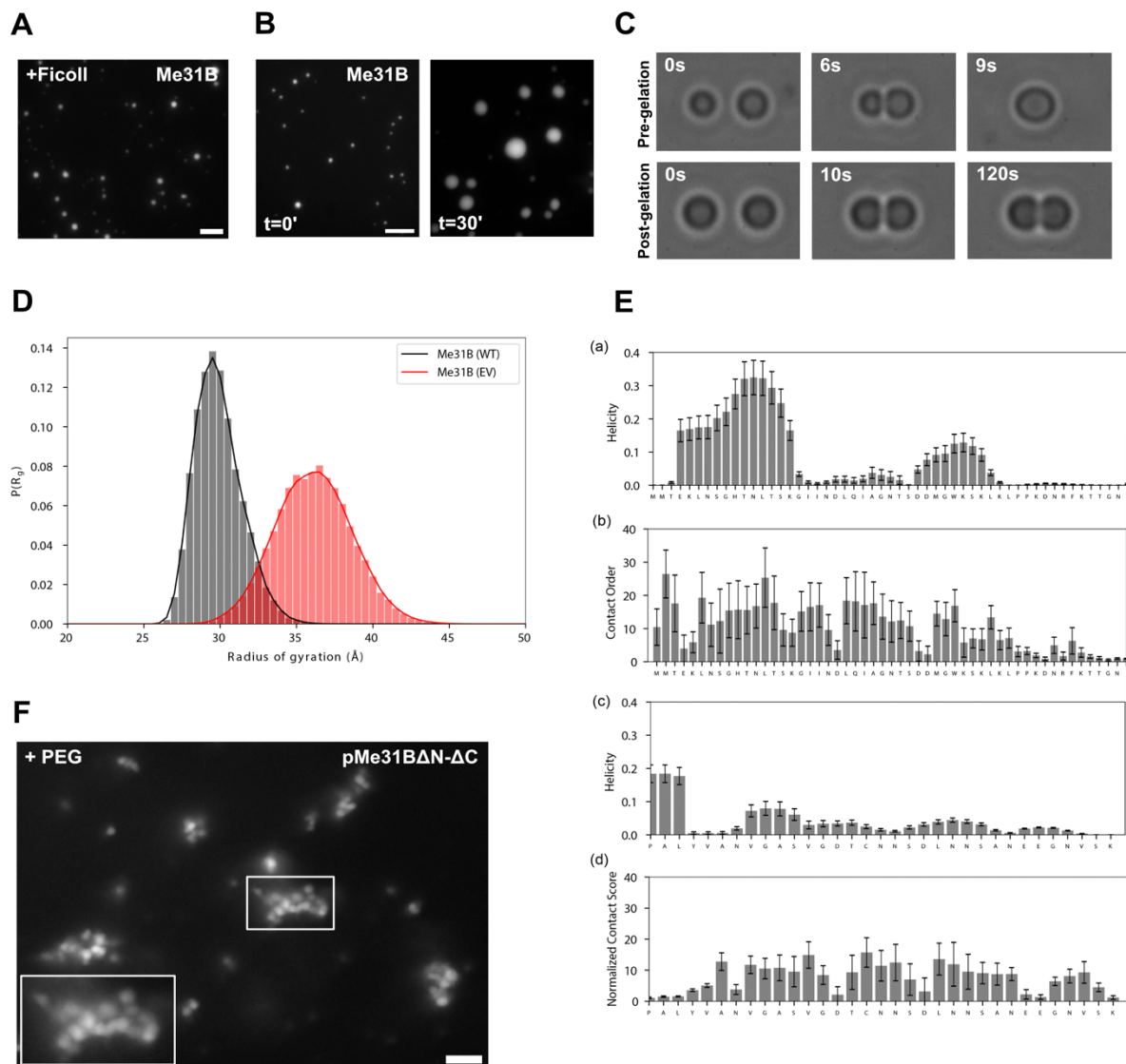
FIGURE S4

Figure S4: Interaction of IDRs with folded domains regulates Me31B physical state *in vitro*

(A) 7.5 μm purified GFP-pMe31B in the presence of 1% Ficoll readily forms phase separated condensates.

(B) Time series of purified GFP-pMe31B (7.5 μm) shows increase in size of condensates over 30 minutes.

(C) Time series of GFP-pMe31B condensate coalescence using optical traps. Rapid fusion of condensates is observed pre-gelation while condensates fail to fuse post-gelation.

(D) Black bars show the Rg distribution for full-length Me31B under standard simulation conditions (full Hamiltonian (WT)), while red bars show the analogous

613 distribution of the radius of gyration for simulations performed in which all attractive

614 interactions are turned off (excluded volume (EV)). The full Hamiltonian simulations

615 are substantially more compact, with an ensemble average radius of gyration of 30.1

616 Å, compared to 36.4 Å for the EV simulations. This compaction of the global

617 dimensions originates from favorable interaction between the two IDRs and the folded

618 domains.

619 **(E)** Local helicity (a,c) and intramolecular contacts (b,d) quantified on a per-residue

620 basis for the NTD (a,b) and CTD (c,d). The NTD possess two short transient helices

621 (4-17 and 31-37), while the CTD is entirely devoid of secondary structures. The NTD

622 engages in more extensive intramolecular interactions than the CTD, as quantified by

623 the normalized contact score (d) (see methods, larger values mean more contacts per

624 residue). In both cases, the IDRs engage relatively uniformly, as opposed to via a

625 specific motif. This implies broad and non-specific interactions between the IDRs and

626 the folded domains.

627 **(F)** pMe31B with both IDRs deleted (pMe31B ΔN-ΔC), in the presence of 1% PEG,

628 fails to coalesce and rather forms amorphous aggregates.

629 Scale bar = 5μm (A,B,F), 1.5 μm (C).
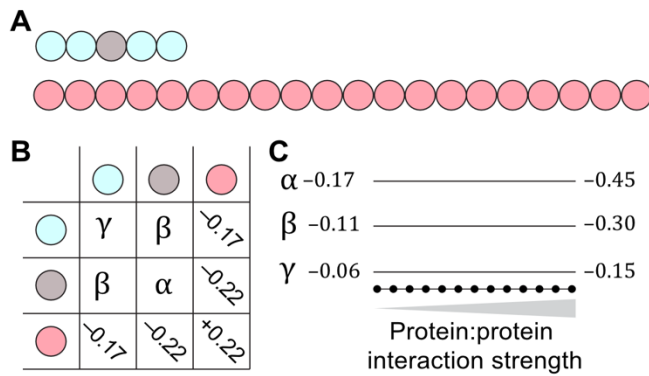
630 **FIGURE S5**

631 **Figure S5: Schematic of course–grained simulations**

632 **(A)** Topology of Me31b (top) and RNA (bottom) molecules used in coarse-grained

633 simulations**.**

634 **(B)** Basic interaction table showing relative bead-bead interaction strengths with

635 protein:protein bead interactions defined in terms of parameters.

636 **(C)** Protein:protein interaction parameters scale uniformly between max and min

637 values.

MATERIALS AND METHODS

***Drosophila* stocks**

The following transgenic lines were used in this paper:

Me31B::GFP (BL 51530, (Buszczak et al., 2007)), *hsp83-MCP-RFP* and *bcd-(ms2)$_6$*

(Weil et al., 2006), GFP::Tral (DGRC 110584, (Morin et al., 2001)), *tral^1* (BDSC 14933)

and *Df(3L)ED4483* (BDSC 8070) (Wilhelm et al., 2005).

Fly stocks were maintained at 25ºC on Iberian recipe fly food as per standard procedure. For mature oocytes experiments, female flies were fed on yeast for two days at 25ºC prior to dissection.

Sample preparation

Mature oocytes from fattened female flies were dissected into halocarbon oil on a 22mm by 40mm cover slip for live imaging. For extrusion assays, membranes of dissected mature oocytes were poked and ruptured using sharp forceps to extrude the oocyte contents into the oil. Extruded material was then subjected to live imaging.

Live imaging

Live imaging of *in vivo* and *ex vivo* P bodies, including all Fluorescent Recovery After Photobleaching experiments, were performed on the Olympus FV3000 microscope using the 1.35 NA, 60X silicone objective. Live imaging of recombinant Me31B condensates, induced on 35mm glass bottom MatTek dishes, was performed on the DeltaVision Core widefield microscope using a 1.4 NA, 60X oil immersion objective.

Pharmacological treatments

Mature oocytes mounted in oil on a 22 by 40mm coverslip and set up under the microscope were treated with one or two drops of 10 µg/ml cytochalasin-D (Sigma-Aldrich) or 5% 1,6 hexanediol (Sigma-Aldrich) or 500ng/ml RNase A (Sigma-Aldrich) mixed in 1X Dulbecco's Phosphate-buffered saline (PBS) solution without MgCl$_2$ (Sigma-Aldrich), or home-made activation buffer (3.3mM NaH$_2$PO$_4$, 16.6mM KH$_2$PO$_4$, 10mM NaCl, 50mM KCl, 5% PEG 8000, 2mM CaCl$_2$, pH 6.4; York-andersen *et al.*, 2015) using a glass pipette. Me31B or Tral labelled P bodies before and after treatment were then imaged. For salt experiments, mature oocytes were extruded into various concentrations of MgCl$_2$ or NaCl mixed in 1X PBS for 15 minutes before being subjected to live imaging. In the case of excessive movement of the oocytes or

669 extruded material during addition of solutions, the focal plane of interest was adjusted

670 accordingly, and imaging was performed.

Protein purification

672 Recombinant GFP-Me31B, both the wild-type (WT) and the Me31BΔN-ΔC (mutant),

673 were expressed in and purified from insect cells using the FlexiBAC baculovirus vector

674 system (Lemaitre et al. 2019). Cell lysis was performed using a LM20 microfluidizer in

675 lysis buffer containing 50mM Tris/HCl pH 7.6, 2mM EDTA, 1x EDTA-containing

676 protease inhibitor cocktail (Roche), 1M KCl, 5% glycerol, 10mM imidazole, 3 ug/L

677 Benzonase, 1 mM DTT. The soluble lysate fraction was collected after centrifugation

678 for 1 hour at 16000 rpm (Beckman Coulter JA-25.50) at 4ºC. MBP-tagged protein was

679 captured by gravity flow affinity chromatography using amylose resin (New England

680 Biolabs). Captured protein was washed with wash buffer (50mM Tris/HCl pH 7.6, 2mM

681 EDTA,1M KCl, 5% glycerol, 10mM imidazole, 1 mM DTT, 3 ug/L Benzonase) and

682 eluted using wash buffer containing 20mM maltose. The eluted protein was incubated

683 with GST 3C- precision protease (1:50) at room temperature for 2 hours to cleave off

684 affinity tags. Samples were applied to size exclusion chromatography using a HiLoad

685 16/600 Superdex 200 pg (GE Life Sciences) on an Akta pure chromatography system

686 in 50mM Tris/HCl pH 7.6, 2mM EDTA,1M KCl, 5% glycerol, 1 mM DTT. Proteins were

687 finally concentrated using an Amicon Ultra centrifugal-500-30K filter at 4000 xg.

688 Aliquots were flash frozen and stored at -80ºC.

In vitro **phase separation assay**

690 Stored protein samples were thawed and spun to remove any residual precipitates.

691 To induce phase separation of Me31B condensates (WT and mutant), 7.5 µM

692 recombinant GFP-Me31B protein was added to an eppendorf tube containing the

693 phase separation buffer(50mM KCl, 20mM PIPES, pH 7, 1% PEG-3K). Note: Gentle

694 tapping of the tube induced phase separated, spherical condensates. Avoid mixing the

695 content with a pipette tip as it induces aggregate formation.

Optical tweezer experiments

697 Condensate fusions for wildtype or mutant condensates were quantified using a

698 custom built dual-trap optical tweezer instrument (Jahnel et al., 2011). Condensates

699 were induced in the phase separation buffer containing 5% PEG-3K at the following

700 concentrations protein concentrations: For both WT and mutant condensates, 20 µM

701 Me31B was used. Post condensation, two condensates were trapped using two
702 separate optical traps and brought into close contact to induce fusion.

703 For quantifying the scaled fusion time for WT condensates, firstly, a relaxation time
704 constant was derived from the fusion process over time. The scaled fusion time was
705 then calculated by dividing the time constant by condensate radii to express the fusion
706 time as a function independent of condensate size. For mutant condensates, due to
707 their rapid aggregation post condensation, fusion was not quantifiable.

Fluorescence Recovery After Photobleaching (FRAP)

709 For whole FRAP, Me31B/Tral labeled P bodies or *in vitro* Me31B condensates were
710 entirely photobleached for 5 seconds using 40% laser intensity from the 405nm laser
711 channel. For internal FRAP, a small region within Me31B labeled *in vivo* P bodies or
712 *in vitro* Me31B condensates was photobleached for 5 seconds using 40% laser
713 intensity from the 405nm laser channel. Time lapse series of Me31B fluorescence
714 recovery was recorded every 30 seconds (*in vivo* P bodies) or 10 seconds (*in vitro*
715 Me31B condensates) using the pre-bleach imaging parameters (minimal laser
716 intensity using the 488nm laser channel, 2 Airy unit pinhole, 2048*2048 pixels). Mean
717 fluorescence intensities were estimated using the Fiji ImageJ software. For whole
718 FRAP analysis, background correction was performed by dividing Me31B fluorescent
719 intensities of bleached condensates by fluorescent intensities of unbleached,
720 cytoplasm. For internal FRAP, background correction was performed by dividing
721 Me31B fluorescent intensities of bleached region within condensates by fluorescent
722 intensities of whole condensates.

723 For all FRAP series, statistical analysis, curve fitting and plotting was performed using
724 Rstudio/R software. Data for each condition was averaged and standard deviation was
725 calculated where applicable. Recovery fitting of the normalized mean intensity as
726 function of time was fitted by the least square analysis to determine fit to the single
727 exponential equation: Normalized intensity = $P \times (1 - e^{(-t/\tau)}) + y_0$ where y_0 is the
728 recovery plateau, t is time, τ is the time constant and P is the amplitude of the
729 fluorescence change.

730 To infer the spatiotemporal pattern of fluorescence recovery, kymographs were
731 produced using the ImageJ plugin 'reslice' by measuring fluorescence across of a
732 region of interest over time.

Fluorescence intensity measurements

Analysis of Me31B and *bcd* fluorescence before and after 1,6-HD treatment was performed using ImageJ processing software. Identical imaging parameters were utilized during imaging and measurement of fluorescence using 'analyze particles' and 'measure' feature on ImageJ. Individual Me31B and *bcd* particles were manually counted and analyzed before and after treatment with 1,6-HD.

All-atom simulations

All-atom simulations were run with the ABSINTH implicit solvent model and the CAMPARI Monte Carlo simulation (V3.0) (http://campari.sourceforge.net/V3/index.html) and with the ion parameters derived by Mao *et al* (Mao and Pappu, 2012; Vitalis and Pappu, 2009). Preferential sampling is used such that the backbone dihedral angles of folded domains are held fixed, while all sidechain dihedral angles and the backbone dihedrals of folded proteins are fully sampled. In this way we *a priori* ensure that the folded domains remain folded. While the combination of ABSINTH and CAMPARI is well-established route to obtain reliable ensembles of disordered regions, more positional restraints on folded domains have been used previously applied to obtain good agreement with experiment (Cubuk et al., 2020; Martin and Mittag, 2018; Martin et al., 2020; Newcombe et al., 2018).

Starting structures were generated first by constructing homology models of Me31B based on the DDX6 structure (PDB: 4CT5) using SWISS-MODEL (Waterhouse et al., 2018). N- and C-terminal IDRs were constructed using CAMPARI. For all simulations, disordered regions were started from randomly generated non-overlapping random-coil conformations, with each replica using a unique starting structure. Monte Carlo simulations evolve the system via a series of moves that perturb backbone and sidechain dihedral angles along with the rigid-body coordinates of both polypeptides and explicit ions. Simulation analysis was performed using CAMPARITraj (www.ctraj.com) and MDTraj (McGibbon et al., 2015). The protein secondary structure was assessed using the DSSP algorithm (Kabsch and Sander, 1983).

Contact score analysis was performed by assessing the fraction of simulations in which two residues were in direct contact, a distance calibrated as 5.0 Å or shorter between heavy atoms. This fraction was divided by the analogous fraction computed from simulations in which all attractive molecular interactions (solvation effects,

765 electrostatics, attractive component of the Lennard-Jones potential) were set to 0.0, in
766 the so-called excluded volume (EV) limit (Holehouse et al., 2015).

767 All simulations were run at 10 mM NaCl and 310 K. Fifty independent simulations were
768 run for a total of 80 million Monte Carlo steps with 5 million steps for equilibration. The
769 system state saved every 100,000 steps. Each simulation generated 750 frames,
770 generating a final ensemble of 37,500 frames. Where included, error bars are standard
771 error of the mean over the fifty independent simulations.

772 **Bioinformatics**
773 Disordered regions were calculated using both Mobidb-lite 1 and with metapredict 2,3.
774 Disordered regions were identified using consensus scores from Mobidib-lite with a
775 minimum IDR length of 25 residues and 3 or more predictors predicting a region to be
776 disordered. The raw set of disordered regions from the drosophila proteome, along
777 with analogous data for P body proteins is provided in the supplementary repository:
778 https://github.com/holehouse-
779 lab/supportingdata/tree/master/2021/sankaranarayanan_me31b_2021.
780 Sequence analysis was performed using localCIDER4,5.

781 **Coarse-grained simulations**
782 Coarse-grained simulations were performed with the PIMMS simulation engine. 6,7.
783 Lattice-based Monte Carlo simulations afford a computationally tractable approach to
784 sample systems with coexisting liquid phases, as has been applied in several different
785 contexts 7–10. Monte Carlo moves include chain translate, rotate, and local/global
786 pivot moves.

787 Simulations were run using a simple representation scheme in which Me31b was
788 represented as a five-bead model made up of two N-terminal beads, a single central
789 bead, and two C-terminal beads (Figure S4GA). In this way, the protein consists of
790 intrinsically disordered region (IDR) beads and ordered domain (OD) beads. RNA is
791 represented as a 20-bead homopolymer (Figure S4GA). We emphasize that these
792 models are designed to describe a class of phenomenon, as opposed to capturing
793 features specific to Me31b over RNA binding proteins. Our simplification of RNA and
794 protein not-withstanding, these simple models allow us to interrogate general
795 behavior.

796   The strength of interactions between the three bead types is shown in Figure S4GB

797   and SXC. Units are in per kT (where k=1). The core keyfiles and parameter files used

798   to run these simulations are provided at https://github.com/holehouse-

799   lab/supportingdata/tree/master/2021/sankaranarayanan_me31b_2021.

800   For protein:RNA and RNA:RNA interaction strengths are held fixed across all

801   simulations, while the protein:protein interaction strength is systematically altered

802   across the simulations shown in Figure S4GC. The specific interaction strengths were

803   chosen to qualitatively reflect insights from experimental work - i.e. OD:OD interaction

804   is stronger than OD:IDR interaction, with IDR:IDR interaction being the weakest. We

805   also assume both OD and IDR beads can interact with RNA, and that RNA:RNA

806   interaction is repulsive. As a final note, we anticipate that RNA:RNA interactions plays

807   an additional role in P body stability, assembly, and disassembly. However, for our

808   initial simple model, absent of other specific information, we avoided adding more

809   tunable parameters to develop a simple yet physically reasonable.

810   All simulations were run with 800 Me31b protein molecules. Simulations with RNA

811   were also run with 50 RNA molecules. These numbers were chosen to ensure that

812   reasonable statistics on droplet recruitment could be obtained with a sufficiently large

813   system where bona fide phase separation occurs. Simulations were run on a 60 x 60

814   x 60 lattice with periodic boundary conditions, and simulation analysis was performed

815   on the terminal 20% of the frames. Simulations were run for around 2.5 billion Monte

816   Carlo moves, and three independent replicas were performed, such that error bars are

817   the standard error of the mean on these replicas.

ACKNOWLEDGEMENTS

AUTHOR CONTRIBUTIONS

829 M.S. performed the majority of experiments. M.S. and T.T.W. designed the majority of
830 the experiments. R.J.E. and A.S.H. performed all simulations and *in silico* modeling.
831 I.R.E.A.T. assisted with protein purification. M.J. performed the optical tweezer
832 experiments. M.S., R.J.E., M.J., M.W., and A.S.H. analyzed the data. M.S. and T.T.W.
833 wrote the manuscript. M.S., A.S.H., S.A. and T.T.W. edited the manuscript.

CONFLICT OF INTERESTS

835 S.A. is an advisor on the scientific advisory board of Dewpoint Therapeutics. A.S.H.
836 is a scientific consultant with Dewpoint Therapeutics.

REFERENCES

1. Andersen, A.H.Y., Wolfner, M.F., Wood, B.W., and Weil, T.T. (2020). A calcium - mediated actin redistribution at egg activation in Drosophila. 293–304.

2. Andrei, M.A., Ingelfinger, D., Heintzmann, R., Achsel, T., Rivera-pomar, R., and Lührmann, R. (2005). A role for eIF4E and eIF4E-transporter in targeting mRNPs to mammalian processing bodies. 717–727.

3. Bakthavachalu, B., Huelsmeier, J., Sudhakaran, I.P., Hillebrand, J., Singh, A., Petrauskas, A., Thiagarajan, D., Sankaranarayanan, M., Mizoue, L., Anderson, E.N., et al. (2018). RNP-Granule Assembly via Ataxin-2 Disordered Domains Is Required for Long-Term Memory and Neurodegeneration. Neuron *98*, 754-766.e4.

4. Banani, S.F., Lee, H.O., Hyman, A.A., and Rosen, M.K. (2017). Biomolecular condensates: Organizers of cellular biochemistry. Nat. Rev. Mol. Cell Biol. *18*, 285–298.

5. Boeynaems, S., Alberti, S., Fawzi, N.L., Mittag, T., Polymenidou, M., Rousseau, F., Schymkowitz, J., Shorter, J., Wolozin, B., Van Den Bosch, L., et al. (2018). Protein Phase Separation: A New Phase in Cell Biology. Trends Cell Biol. *28*, 420–435.

6. Boeynaems, S., Holehouse, A.S., Weinhardt, V., Kovacs, D., Van Lindt, J., Larabell, C., Bosch, L. Van Den, Das, R., Tompa, P.S., Pappu, R. V., et al. (2019). Spontaneous driving forces give rise to protein−RNA condensates with coexisting phases and complex material properties. Proc. Natl. Acad. Sci. U. S. A. *116*, 7889–7898.

7. Boke, E., Ruer, M., Wühr, M., Coughlin, M., Lemaitre, R., Gygi, S.P., Alberti, S., Drechsel, D., Hyman, A.A., and Mitchison, T.J. (2016). Amyloid-like Self-Assembly of a Cellular Compartment. Cell *166*, 637–650.

8. Bouveret, E. (2000). A Sm-like protein complex that participates in mRNA degradation. EMBO J. *19*, 1661–1671.

9. Brangwynne, C.P., Eckmann, C.R., Courson, D.S., Rybarska, A., Hoege, C., Gharakhani, J., Jülicher, F., and Hyman, A.A. (2009). Germline P granules are liquid droplets that localize by controlled dissolution/condensation. Science (80-.).

867   *324*, 1729–1732.

868   10. Brangwynne, C.P., Mitchison, T.J., and Hyman, A.A. (2011). Active liquid-like
869   behavior of nucleoli determines their size and shape in Xenopus laevis oocytes.
870   Proc. Natl. Acad. Sci. U. S. A. *108*, 4334–4339.

871   11. Brangwynne, C.P., Tompa, P., and Pappu, R. V. (2015). Polymer physics of
872   intracellular phase transitions. Nat. Phys. *11*, 899–904.

873   12. Buchan, J.R., Buchan, R., and Buchan, J.R. (2014). mRNP granules Assembly,
874   function , and connections with disease. *6286*.

875   13. Buszczak, M., Paterno, S., Lighthouse, D., Bachman, J., Planck, J., Owen, S.,
876   Skora, A.D., Nystul, T.G., Ohlstein, B., Allen, A., et al. (2007). The carnegie protein
877   trap library: a versatile tool for Drosophila developmental studies. Genetics *175*,
878   1505–1531.

879   14. Cubuk, J., Alston, J.J., Incicco, J.J., Singh, S., Stuchell-Brereton, M.D., Ward,
880   M.D., Zimmerman, M.I., Vithani, N., Griffith, D., Wagoner, J.A., et al. (2020). The
881   SARS-CoV-2 nucleocapsid protein is dynamic, disordered, and phase separates
882   with RNA. BioRxiv.

883   15. Dorone, Y., Boeynaems, S., Jin, B., Bossi, F., Flores, E., and Lazarus, E. (2020).
884   Hydration-dependent phase separation of a prion-like protein regulates seed
885   germination during water stress .

886   16. Dzuricky, M., Rogers, B.A., Shahid, A., Cremer, P.S., and Chilkoti, A. (2020). using
887   artificial disordered proteins. Nat. Chem. *12*.

888   17. Eichhorn, S.W., Subtelny, A.O., Kronja, I., Kwasnieski, J.C., Orr-Weaver, T.L., and
889   Bartel, D.P. (2016). mRNA poly(A)-tail changes specified by deadenylation broadly
890   reshape translation in Drosophila oocytes and early embryos. Elife *5*, 1–24.

891   18. Eulalio, A., Behm-Ansmant, I., Schweizer, D., and Izaurralde, E. (2007). P-Body
892   Formation Is a Consequence, Not the Cause, of RNA-Mediated Gene Silencing.
893   Mol. Cell. Biol. *27*, 3970–3981.

894   19. Feric, M., Vaidya, N., Harmon, T.S., Mitrea, D.M., Zhu, L., Richardson, T.M.,
895   Kriwacki, R.W., Pappu, R. V., and Brangwynne, C.P. (2016). Coexisting Liquid
896   Phases Underlie Nucleolar Subcompartments. Cell *165*, 1686–1697.

897   20. Franzmann, T.M., Jahnel, M., Pozniakovsky, A., Mahamid, J., Holehouse, A.S.,
898   Nüske, E., Richter, D., Baumeister, W., Grill, S.W., Pappu, R. V., et al. (2018).
899   Phase separation of a yeast prion protein promotes cellular fitness. Science (80).
900   *359*.

901   21. Götze, M., Dufourt, J., Ihling, C., Rammelt, C., Pierson, S., Sambrani, N., Temme,
902   C., Sinz, A., Simonelig, M., and Wahle, E. (2017). Translational repression of the
903   Drosophila nanos mRNA involves the RNA helicase Belle and RNA coating by
904   Me31B and Trailer hitch. 1552–1568.

905   22. Hara, M., Lourido, S., Petrova, B., Lou, H.J., Von Stetina, J.R., Kashevsky, H.,
906   Turk, B.E., and Orr-Weaver, T.L. (2018). Identification of PNG kinase substrates
907   uncovers interactions with the translational repressor TRAL in the oocyte-to-
908   embryo transition. Elife *7*, 1–19.

909   23. Holehouse, A.S., Garai, K., Lyle, N., Vitalis, A., and Pappu, R. V (2015).
910   Quantitative assessments of the distinct contributions of polypeptide backbone
911   amides versus side chain groups to chain expansion via chemical denaturation. J.
912   Am. Chem. Soc. *137*, 2984–2995.

913   24. Hondele, M., Sachdev, R., Heinrich, S., Wang, J., Vallotton, P., Fontoura, B.M.A.,
914   and Weis, K. (2019). DEAD-box ATPases are global regulators of phase-separated
915   organelles. Nature *573*, 144–148.

916   25. Hubstenberger, A., Noble, S.L., Cameron, C., and Evans, T.C. (2013). Translation
917   repressors, an RNA helicase, and developmental cues control RNP phase
918   transitions during early development. Dev. Cell *27*, 161–173.

919   26. Hubstenberger, A., Courel, M., Bénard, M., Souquere, S., Ernoult-Lange, M.,
920   Chouaib, R., Yi, Z., Morlot, J.B., Munier, A., Fradet, M., et al. (2017). P-Body
921   Purification Reveals the Condensation of Repressed mRNA Regulons. Mol. Cell
922   *68*, 144-157.e5.

923   27. Hyman, A.A., Weber, C.A., and Jülicher, F. (2014). Liquid-Liquid Phase Separation
924   in Biology. Annu. Rev. Cell Dev. Biol. *30*, 39–58.

925   28. Jahnel, M., Behrndt, M., Jannasch, A., Schäffer, E., and Grill, S.W. (2011).
926   Measuring the complete force field of an optical trap. Opt. Lett. *36*, 1260–1262.

29. Jung, H., Gkogkas, C.G., Sonenberg, N., and Holt, C.E. (2014). Review Remote Control of Gene Function by Local Translation. Cell *157*, 26–40.

30. Kabsch, W., and Sander, C. (1983). Dictionary of protein secondary structure: pattern recognition of hydrogen-bonded and geometrical features. Biopolymers *22*, 2577–2637.

31. Kaneuchi, T., Sartain, C. V, Takeo, S., Horner, V.L., Buehner, N.A., and Aigaki, T. (2015). Calcium waves occur as Drosophila oocytes activate. *112*, 791–796.

32. Kato, M., Han, T.W., Xie, S., Shi, K., Du, X., Wu, L.C., Mirzaei, H., Goldsmith, E.J., Longgood, J., Pei, J., et al. (2012). Cell-free formation of RNA granules: Low complexity sequence domains form dynamic fibers within hydrogels. Cell *149*, 753–767.

33. Kedersha, N., Stoecklin, G., Ayodele, M., Yacono, P., Lykke-andersen, J., Marvin, J.F., Scheuner, D., Kaufman, R.J., Golan, D.E., and Anderson, P. (2005). Stress granules and processing bodies are dynamically linked sites of mRNP remodeling 4. *169*, 871–884.

34. Kloc, M., and Etkin, L.D. (2005). RNA localization mechanisms in oocytes. J. Cell Sci. *118*, 269–282.

35. Krauchunas, A.R., and Wolfner, M.F. (2013). Molecular Changes During Egg Activation. Curr. Top. Dev. Biol. *102*, 267–292.

36. Kroschwald, S., Maharana, S., Mateju, D., Malinovska, L., Nüske, E., Poser, I., Richter, D., and Alberti, S. (2015). Promiscuous interactions and protein disaggregases determine the material state of stress-inducible RNP granules. Elife *4*, 1–32.

37. Kroschwald, S., Munder, M.C., Maharana, S., Ruer, M., Hyman, A.A., Alberti, S., Kroschwald, S., Munder, M.C., Maharana, S., Franzmann, T.M., et al. (2018). Different Material States of Pub1 Condensates Define Distinct Modes of Stress Adaptation and Article Different Material States of Pub1 Condensates Define Distinct Modes of Stress Adaptation and Recovery. CellReports *23*, 3327–3339.

38. Lasko, P. (2012). mRNA localization and translational control in Drosophila oogenesis. Cold Spring Harb. Perspect. Biol. *4*, 1–15.

39. Li, P., Banjade, S., Cheng, H.C., Kim, S., Chen, B., Guo, L., Llaguno, M., Hollingsworth, J. V., King, D.S., Banani, S.F., et al. (2012). Phase transitions in the assembly of multivalent signalling proteins. Nature *483*, 336–340.

40. Lin, M. Der, Jiao, X., Grima, D., Newbury, S.F., Kiledjian, M., and Chou, T. Bin (2008). Drosophila processing bodies in oogenesis. Dev. Biol. *322*, 276–288.

41. Lin, Y., Protter, D.S.W., Rosen, M.K., and Parker, R. (2015a). Formation and Maturation of Phase-Separated Liquid Droplets by RNA-Binding Proteins. Mol. Cell *60*, 208–219.

42. Lin, Y., Protter, D.S.W., Rosen, M.K., and Parker, R. (2015b). Formation and Maturation of Phase-Separated Liquid Droplets by RNA-Binding Proteins. Mol. Cell *60*, 208–219.

43. Luo, Y., Na, Z., and Slavoff, S.A. (2018). P-Bodies: Composition, Properties, and Functions. Biochemistry *57*, 2424–2431.

44. Lyon, A.S., Peeples, W.B., and Rosen, M.K. (2021). P H A S E S E PA R AT I O N I N B I O LO G Y. Nat. Rev. Mol. Cell Biol. *22*.

45. Majumdar, A., Cesario, W.C., White-Grindley, E., Jiang, H., Ren, F., Khan, M. "Repon," Li, L., Choi, E.M.-L., Kannan, K., Guo, F., et al. (2012). Critical Role of Amyloid-like Oligomers of Drosophila Orb2 in the Persistence of Memory. Cell *148*, 515–529.

46. Mao, A.H., and Pappu, R. V (2012). Crystal lattice properties fully determine short-range interaction parameters for alkali and halide ions. J. Chem. Phys. *137*, 64104.

47. Martin, E.W., and Mittag, T. (2018). Relationship of Sequence and Phase Separation in Protein Low-Complexity Regions. Biochemistry *57*, 2478–2487.

48. Martin, E.W., Holehouse, A.S., Peran, I., Farag, M., Incicco, J.J., Bremer, A., Grace, C.R., Soranno, A., Pappu, R. V., and Mittag, T. (2020). Valence and patterning of aromatic residues determine the phase behavior of prion-like domains. Science (80-.). *367*, 694–699.

49. McCambridge, A., Solanki, D., Olchawa, N., Govani, N., Trinidad, J.C., and Gao, M. (2020). Comparative Proteomics Reveal Me31B's Interactome Dynamics, Expression Regulation, and Assembly Mechanism into Germ Granules during

987   Drosophila Germline Development. Sci. Rep. *10*, 1–13.

988   50. McGibbon, R.T., Beauchamp, K.A., Harrigan, M.P., Klein, C., Swails, J.M.,
989   Hernández, C.X., Schwantes, C.R., Wang, L.-P., Lane, T.J., and Pande, V.S.
990   (2015). MDTraj: A Modern Open Library for the Analysis of Molecular Dynamics
991   Trajectories. Biophys. J. *109*, 1528–1532.

992   51. Medioni, C., Mowry, K., and Besse, F. (2012). Principles and roles of mRNA
993   localization in animal development. Dev. *139*, 3263–3276.

994   52. Mitrea, D.M., Cika, J.A., Guy, C.S., Ban, D., Banerjee, P.R., Stanley, C.B., Nourse,
995   A., Deniz, A.A., and Kriwacki, R.W. (2016). Nucleophosmin integrates within the
996   nucleolus via multi-modal interactions with proteins displaying R-rich linear motifs
997   and rRNA. 1–33.

998   53. Monzo, K., Papoulas, O., Cantin, G.T., Wang, Y., Yates, J.R., and Sisson, J.C.
999   (2006). Fragile X mental retardation protein controls trailer hitch expression and
1000   cleavage furrow formation in Drosophila embryos. Proc. Natl. Acad. Sci. U. S. A.
1001   *103*, 18160–18165.

1002 54. Morin, X., Daneman, R., Zavortink, M., and Chia, W. (2001). A protein trap strategy
1003   to detect GFP-tagged proteins expressed from their endogenous loci in Drosophila.
1004   Proc. Natl. Acad. Sci. U. S. A. *98*, 15050–15055.

1005 55. Murthy, A.C., Dignon, G.L., Kan, Y., Zerze, G.H., Parekh, S.H., Mittal, J., and
1006   Fawzi, N.L. (2019). Molecular interactions underlying liquid − liquid phase
1007   separation of the FUS low-complexity domain. Nat. Struct. Mol. Biol. *26*.

1008 56. Nakamura, A., Amikura, R., Hanyu, K., and Kobayashi, S. (2001). Me31B silences
1009   translation of oocyte-localizing RNAs through the formation of cytoplasmic RNP
1010   complex during Drosophila oogenesis. Development *128*, 3233–3242.

1011 57. Newcombe, E.A., Ruff, K.M., Sethi, A., Ormsby, A.R., Ramdzan, Y.M., Fox, A.,
1012   Purcell, A.W., Gooley, P.R., Pappu, R. V, and Hatters, D.M. (2018). Tadpole-like
1013   Conformations of Huntingtin Exon 1 Are Characterized by Conformational
1014   Heterogeneity that Persists regardless of Polyglutamine Length. J. Mol. Biol. *430*,
1015   1442–1458.

1016 58. Nott, T.J., Petsalaki, E., Farber, P., Jervis, D., Fussner, E., Plochowietz, A.,

1017   Craggs, T.D., Bazett-Jones, D.P., Pawson, T., Forman-Kay, J.D., et al. (2015).
1018   Phase Transition of a Disordered Nuage Protein Generates Environmentally
1019   Responsive Membraneless Organelles. Mol. Cell *57*, 936–947.

1020 59. Pak, C.W., Kosno, M., Holehouse, A.S., Padrick, S.B., Mittal, A., Ali, R., Yunus,
1021   A.A., Liu, D.R., Pappu, R. V, and Rosen, M.K. (2016). Sequence Determinants of
1022   Intracellular Phase Separation by Complex Coacervation of a Disordered Protein.
1023   Mol. Cell *63*, 72–85.

1024 60. Parker, R., and Sheth, U. (2007). P Bodies and the Control of mRNA Translation
1025   and Degradation. Mol. Cell *25*, 635–646.

1026 61. Patel, A., Lee, H.O., Jawerth, L., Maharana, S., Jahnel, M., Hein, M.Y., Stoynov,
1027   S., Mahamid, J., Saha, S., Franzmann, T.M., et al. (2015). A Liquid-to-Solid Phase
1028   Transition of the ALS Protein FUS Accelerated by Disease Mutation. Cell *162*,
1029   1066–1077.

1030 62. Patel, S.S., Belmont, B.J., Sante, J.M., and Rexach, M.F. (2007). Natively Unfolded
1031   Nucleoporins Gate Protein Diffusion across the Nuclear Pore Complex. 83–96.

1032 63. Powers, S.K., Holehouse, A.S., Korasick, D.A., Schreiber, K.H., Clark, N.M., Jing,
1033   H., Emenecker, R., Han, S., Tycksen, E., Hwang, I., et al. (2019). Nucleo-
1034   cytoplasmic Partitioning of ARF Proteins Controls Auxin Responses in Arabidopsis
1035   thaliana. Mol. Cell *76*, 177-190.e5.

1036 64. Protter, D.S.W., Rao, B.S., Treeck], B. [Van, Lin, Y., Mizoue, L., Rosen, M.K., and
1037   Parker, R. (2018). Intrinsically Disordered Regions Can Contribute Promiscuous
1038   Interactions to RNP Granule Assembly. Cell Rep. *22*, 1401–1412.

1039 65. Puthanveettil, S. V (2013). RNA transport and long-term memory storage. *6286*.

1040 66. Rajasethupathy, P., Fiumara, F., Sheridan, R., Betel, D., Puthanveettil, S. V,
1041   Russo, J.J., Sander, C., Tuschl, T., and Kandel, E. (2009). Article Characterization
1042   of Small RNAs in Aplysia Reveals a Role for miR-124 in Constraining Synaptic
1043   Plasticity through CREB. Neuron *63*, 803–817.

1044 67. Riback, J.A., Katanski, C.D., Kear-Scott, J.L., Pilipenko, E. V, Rojek, A.E., Sosnick,
1045   T.R., and Drummond, D.A. (2017). Stress-Triggered Phase Separation Is an
1046   Adaptive, Evolutionarily Tuned Response. Cell *168*, 1028-1040.e19.

68. Ribbeck, K., and Go, D. (2002). The permeability barrier of nuclear pore complexes appears to operate via hydrophobic exclusion. *21*.

69. Rog, O., Köhler, S., and Dernburg, A.F. (2017). The synaptonemal complex has liquid crystalline properties and spatially regulates meiotic recombination factors. Elife *6*.

70. Shin, Y., and Brangwynne, C.P. (2017). Liquid phase condensation in cell physiology and disease. Science (80-.). *357*.

71. Sudhakaran, I.P., and Ramaswami, M. (2017). Long-term memory consolidation: The role of RNA- binding proteins with prion-like domains. RNA Biol. *14*, 568–586.

72. Tadros, W., and Lipshitz, H.D. (2009). The maternal-to-zygotic transition: a play in two acts. *3042*, 3033–3042.

73. Tritschler, F., Eulalio, A., Truffault, V., Hartmann, M.D., Helms, S., Schmidt, S., Coles, M., Izaurralde, E., and Weichenrieder, O. (2007). A Divergent Sm Fold in EDC3 Proteins Mediates DCP1 Binding and P-Body Targeting. Mol. Cell. Biol. *27*, 8600–8611.

74. Tritschler, F., Eulalio, A., Helms, S., Schmidt, S., Coles, M., Weichenrieder, O., Izaurralde, E., and Truffault, V. (2008). Similar Modes of Interaction Enable Trailer Hitch and EDC3 To Associate with DCP1 and Me31B in Distinct Protein Complexes. Mol. Cell. Biol. *28*, 6695–6708.

75. Tritschler, F., Braun, J.E., Eulalio, A., Truffault, V., Izaurralde, E., and Weichenrieder, O. (2009). Structural Basis for the Mutually Exclusive Anchoring of P Body Components EDC3 and Tral to the DEAD Box Protein DDX6/Me31B. Mol. Cell *33*, 661–668.

76. Vitalis, A., and Pappu, R. V (2009). ABSINTH: a new continuum solvation model for simulations of polypeptides in aqueous solutions. J. Comput. Chem. *30*, 673–699.

77. Wang, J.T., Smith, J., Chen, B., Schmidt, H., Rasoloson, D., Paix, A., Lambrus, B.G., Calidas, D., Betzig, E., and Seydoux, G. (2014). Regulation of RNA granule dynamics by phosphorylation of serine-rich, intrinsically disordered proteins in C . elegans. 1–23.

78. Wang, M., Ly, M., Lugowski, A., Laver, J.D., Lipshitz, H.D., Smibert, C.A., and Rissland, O.S. (2017). ME31B globally represses maternal mRNAs by two distinct mechanisms during the Drosophila maternal-to-zygotic transition. Elife *6*, 1–22.

79. Waterhouse, A., Bertoni, M., Bienert, S., Studer, G., Tauriello, G., Gumienny, R., Heer, F.T., de Beer, T.A.P., Rempfer, C., Bordoli, L., et al. (2018). SWISS-MODEL: homology modelling of protein structures and complexes. Nucleic Acids Res. *46*, W296–W303.

80. Weber, S.C. (2017). ScienceDirect Sequence-encoded material properties dictate the structure and function of nuclear bodies. Curr. Opin. Cell Biol. *46*, 62–71.

81. Weber, S.C., and Brangwynne, C.P. (2012). Minireview Getting RNA and Protein in Phase. Cell *149*, 1188–1191.

82. Weil, T.T., Forrest, K.M., and Gavis, E.R. (2006). Localization of bicoid mRNA in late oocytes is maintained by continual active transport. Dev. Cell *11*, 251–262.

83. Weil, T.T., Parton, R.M., Herpers, B., Soetaert, J., Veenendaal, T., Xanthakis, D., Dobbie, I.M., Halstead, J.M., Hayashi, R., Rabouille, C., et al. (2012). Drosophila patterning is established by differential association of mRNAs with P bodies. Nat. Cell Biol. *14*, 1305–1313.

84. Wilhelm, J.E., Buszczak, M., and Sayles, S. (2005). Efficient protein trafficking requires trailer hitch, a component of a ribonucleoprotein complex localized to the ER in Drosophila. Dev. Cell *9*, 675–685.

85. Woodruff, J.B., Ferreira Gomes, B., Widlund, P.O., Mahamid, J., Honigmann, A., and Hyman, A.A. (2017). The Centrosome Is a Selective Condensate that Nucleates Microtubules by Concentrating Tubulin. Cell *169*, 1066-1077.e10.

86. York-andersen, A.H., Parton, R.M., Bi, C.J., Bromley, C.L., Davis, I., and Weil, T.T. (2015). RESEARCH ARTICLE A single and rapid calcium wave at egg activation in Drosophila. 553–560.

87. Zhang, H., Elbaum-Garfinkle, S., Langdon, E.M., Taylor, N., Occhipinti, P., Bridges, A.A., Brangwynne, C.P., and Gladfelter, A.S. (2015). RNA Controls PolyQ Protein Phase Transitions. Mol. Cell *60*, 220–230.

MATERIALS AND METHODS REFERENCES

1. Buszczak, M., Paterno, S., Lighthouse, D., Bachman, J., Planck, J., Owen, S., Skora, A.D., Nystul, T.G., Ohlstein, B., Allen, A., et al. (2007). The carnegie protein trap library: a versatile tool for Drosophila developmental studies. Genetics *175*, 1505–1531.

2. Cubuk, J., Alston, J.J., Incicco, J.J., Singh, S., Stuchell-Brereton, M.D., Ward, M.D., Zimmerman, M.I., Vithani, N., Griffith, D., Wagoner, J.A., et al. (2020). The SARS-CoV-2 nucleocapsid protein is dynamic, disordered, and phase separates with RNA. BioRxiv.

3. Holehouse, A.S., Garai, K., Lyle, N., Vitalis, A., and Pappu, R. V (2015). Quantitative assessments of the distinct contributions of polypeptide backbone amides versus side chain groups to chain expansion via chemical denaturation. J. Am. Chem. Soc. *137*, 2984–2995.

4. Jahnel, M., Behrndt, M., Jannasch, A., Schäffer, E., and Grill, S.W. (2011). Measuring the complete force field of an optical trap. Opt. Lett. *36*, 1260–1262.

5. Kabsch, W., and Sander, C. (1983). Dictionary of protein secondary structure: pattern recognition of hydrogen-bonded and geometrical features. Biopolymers *22*, 2577–2637.

6. Mao, A.H., and Pappu, R. V (2012). Crystal lattice properties fully determine short-range interaction parameters for alkali and halide ions. J. Chem. Phys. *137*, 64104.

7. Martin, E.W., and Mittag, T. (2018). Relationship of Sequence and Phase Separation in Protein Low-Complexity Regions. Biochemistry *57*, 2478–2487.

8. Martin, E.W., Holehouse, A.S., Peran, I., Farag, M., Incicco, J.J., Bremer, A., Grace, C.R., Soranno, A., Pappu, R. V., and Mittag, T. (2020). Valence and patterning of aromatic residues determine the phase behavior of prion-like domains. Science (80). *367*, 694–699.

9. McGibbon, R.T., Beauchamp, K.A., Harrigan, M.P., Klein, C., Swails, J.M., Hernández, C.X., Schwantes, C.R., Wang, L.-P., Lane, T.J., and Pande, V.S. (2015). MDTraj: A Modern Open Library for the Analysis of Molecular Dynamics Trajectories. Biophys. J. *109*, 1528–1532.

10. Morin, X., Daneman, R., Zavortink, M., and Chia, W. (2001). A protein trap strategy to detect GFP-tagged proteins expressed from their endogenous loci in Drosophila. Proc. Natl. Acad. Sci. U. S. A. *98*, 15050–15055.

1139   11. Newcombe, E.A., Ruff, K.M., Sethi, A., Ormsby, A.R., Ramdzan, Y.M., Fox, A.,
1140   Purcell, A.W., Gooley, P.R., Pappu, R. V, and Hatters, D.M. (2018). Tadpole-like
1141   Conformations of Huntingtin Exon 1 Are Characterized by Conformational
1142   Heterogeneity that Persists regardless of Polyglutamine Length. J. Mol. Biol. *430*,
1143   1442–1458.
1144   12. Vitalis, A., and Pappu, R. V (2009). ABSINTH: a new continuum solvation model
1145   for simulations of polypeptides in aqueous solutions. J. Comput. Chem. *30*, 673–
1146   699.
1147   13. Waterhouse, A., Bertoni, M., Bienert, S., Studer, G., Tauriello, G., Gumienny, R.,
1148   Heer, F.T., de Beer, T.A.P., Rempfer, C., Bordoli, L., et al. (2018). SWISS-MODEL:
1149   homology modelling of protein structures and complexes. Nucleic Acids Res. *46*,
1150   W296–W303.
1151   14. Weil, T.T., Forrest, K.M., and Gavis, E.R. (2006). Localization of bicoid mRNA in
1152   late oocytes is maintained by continual active transport. Dev. Cell *11*, 251–262.
1153   15. Wilhelm, J.E., Buszczak, M., and Sayles, S. (2005). Efficient protein trafficking
1154   requires trailer hitch, a component of a ribonucleoprotein complex localized to the
1155   ER in Drosophila. Dev. Cell *9*, 675–685.
1156   16. York-andersen, A.H., Parton, R.M., Bi, C.J., Bromley, C.L., Davis, I., and Weil, T.T.
1157   (2015). A single and rapid calcium wave at egg activation in Drosophila. Biology
1158   Open 553–560.